Orbital evidence for clay and acidic sulfate assemblages on Mars based on mineralogical analogs from Rio Tinto, Spain

Orbital Evidence for Clay and Acidic Sulfate Assemblages on Mars Based on Mineralogical Analogs from Rio Tinto, Spain

Hannah H. Kaplan[1]*, Ralph E. Milliken[1], David Fernández-Remolar[2], Ricardo Amils[3], Kevin Robertson[1], and Andrew H. Knoll[4]

Authors:

[1] Department of Earth, Environmental and Planetary Sciences, Brown University, Providence, RI, 02912 USA.

[2]British Geological Survey, Nicker Hill, Keyworth, NG12 5GG, UK.

[3] Centro de Astrobiologia (INTA-CSIC), Ctra Ajalvir km 4, Torrejon de Ardoz, 28850, Spain.

[4] Department of Organismic and Evolutionary Biology, Harvard University, Çambridge, MA, USA.

*Corresponding author: Hannah_Kaplan@Brown.edu

Abstract

Outcrops of hydrated minerals are widespread across the surface of Mars, with clay minerals and sulfates being commonly identified phases. Orbitally-based reflectance spectra are often used to classify these hydrated components in terms of a single mineralogy, although most surfaces likely contain multiple minerals that have the potential to record local geochemical conditions and processes. Reflectance spectra for previously identified deposits in Ius and Melas Chasma within the Valles Marineris, Mars, exhibit an enigmatic feature with two distinct absorptions between 2.2 – 2.3 μm. This spectral 'doublet' feature is proposed to result from a mixture of hydrated minerals, although the identity of the minerals has remained ambiguous. Here we demonstrate that similar spectral doublet features are observed in airborne, field, and laboratory reflectance spectra of rock and sediment samples from Rio Tinto, Spain. Combined visible-near infrared reflectance spectra and X-ray diffraction measurements of these samples reveals that the doublet feature arises from a mixture of Al-phyllosilicate (illite or muscovite) and jarosite. Analyses of orbital data from the Compact Reconnaissance Imaging Spectrometer for Mars (CRISM) shows that the martian spectral equivalents are also consistent with mixtures of Al-phyllosilicates and jarosite, where the Al-phyllosilicate may also include kaolinite and/or halloysite. A case study for a region within Ius Chasma demonstrates that the relative proportions of the Al-phyllosilicate(s) and jarosite vary within one stratigraphic unit as well as between stratigraphic units. The former observation suggests that the jarosite may be a diagenetic (authigenic) product and thus indicative of local pH and redox conditions,

whereas the latter observation may be consistent with variations in sediment flux and/or fluid chemistry during sediment deposition.

Key points:

- A doublet absorption is observed in reflectance spectra of Mars between 2.2 - 2.3 μm.
- Reflectance spectra at Rio Tinto, Spain also show a doublet due to Al-phyllosilicate and jarosite.
- Spectral variation in martian deposits suggests local variation in pH, redox, and/or sediment flux.

Keywords: Mars, surface; Spectroscopy; Infrared observations

1. Introduction

Outcrops of sulfate and clay mineral-bearing rocks are widespread across the ancient surface of Mars [Bibring et al., 2006; Murchie et al., 2009; Ehlmann et al., 2011; Carter et al., 2013], indicating that a complex history of water-rock interaction is preserved in the martian rock record. Visible-near infrared (VIS-NIR) reflectance spectra acquired by the CRISM (Compact Reconnaissance Imaging Spectrometer for Mars) and OMEGA (Observatoire pour la Minéralogie, l'Eau, les Glaces et l'Activité) imaging spectrometers have been used to identify clay minerals in ancient and heavily cratered Noachian terrains [Poulet et al., 2005; Ehlmann et al., 2011; Carter et al., 2013] and thick deposits of sulfates in younger Hesperian terrains and basins [Gendrin et al., 2005; Bibring et al., 2006]. In the cases of Terra Meridiani, Gusev Crater, and Gale Crater, these minerals have been examined *in situ* by rover-based payloads, providing detailed local geologic context for some of these orbital detections [e.g. Klingelhofer et al., 2004; Squyres et al., 2004; Arvidson et al., 2008; Wang et al., 2006; Vaniman et al., 2014].

Many of these orbiter-based detections of hydrated minerals on Mars are discussed in terms of single minerals. That is, the reflectance spectra of these deposits are commonly discussed or interpreted as specific clay, sulfate, or other hydrated minerals (see Ehlmann et al., 2009 for an exception with regards to mineral assemblages at Nili Fossae). Though these deposits are undoubtedly polymineralic, it appears that in many cases a single mineral can be *spectrally* dominant even at the spatial resolution of instruments such as CRISM (e.g., ~18

m/pixel). Therefore, those regions on Mars whose reflectance spectra cannot clearly be attributed to a single dominant hydrated mineral are of particular interest as they may record different and more diverse geological processes than are typically recognized from CRISM data.

Reflectance spectra of deposits and strata within the Valles Marineris reveal a number of locations that fall within this category, and these are the focus of this study. Specifically, CRISM spectra of various deposits within Ius, Melas, and other chasmata exhibit an absorption feature with local minima centered at ~2.21 and ~2.27 μm [Metz et al., 2009; Roach et al., 2010; Weitz et al., 2011] (Figure 1). The spectral shape and properties of this absorption feature, which we will refer to as a spectral 'doublet', does not match the spectrum of any single common mineral in existing spectral libraries, suggesting it likely cannot be attributed to a single type of clay, sulfate, or other common hydrated mineral.

Previous studies have hypothesized that this material represents a mixture of clays, sulfates (possibly including jarosite), and/or poorly crystalline phases [Roach et al., 2010; Tosca et al., 2008b; Noe Dobrea et al., 2011; Weitz et al., 2014], but the exact assemblage remains unknown. We have observed that similar spectral features occur in airborne, field, and lab spectra of rocks and sediments at Rio Tinto, Spain, which has been previously studied as a Mars analog due to the river's acidity, iron hydrochemistry, and extensive iron oxide deposits [Fernandez-Remolar et al. 2003]. Indeed, it has been suggested that the ferric iron and sulfate mineralogy

produced by the acidic waters may be analogous to conditions experienced in Terra Meridiani during the Hesperian [Fernandez-Remolar et al., 2004], and similar conditions may also have occurred in portions of the Valles Marineris [e.g., Bibring et al., 2007].

In this study we integrate airborne, *in situ*, and lab measurements to characterize a suite of samples from different sites at Rio Tinto to understand the mineralogical origin of the 'doublet' spectral signature, and we then compare our findings to reflectance spectra acquired by the CRISM instrument for deposits in Valles Marineris, Mars. We demonstrate that the doublet absorptions observed in samples from Rio Tinto are comparable to the spectral signatures observed in Valles Marineris, that the former are the result of Al-bearing phyllosilicates mixed with jarosite, and that similar mineral assemblages may be present on Mars. This indicates Rio Tinto contains materials that can serve as mineralogical and spectral analogs for the martian deposits, though the geological processes that lead to the formation of these assemblages on Earth and Mars need not be equivalent. Specifically, although jarosite and Al-phyllosilicates may co-occur in geologic units today on Mars, this association does not require their formation environments to have been the same in space and/or time. Both mineral types may be authigenic or detrital, and detailed geologic context is necessary to distinguish between these options and the associated implications for local paleoenvironmental conditions.

2. Background

2.1 Overview of Clay and Sulfate Detections on Mars

The most commonly observed spectral signatures on Mars that have been interpreted as clay minerals are identified as Fe/Mg smectite, but mixed-layer clays, chlorite, Al-smectite, mica, kaolinite, and serpentine have also been observed [Mustard et al., 2008; Murchie et al., 2009; Ehlmann et al., 2011; Carter et al., 2013]. Aqueous alteration of basaltic protoliths both at the surface and in the subsurface have been invoked as the major source of these clay minerals, although subsequent erosion and eolian/fluvial transport has led to their occurrence in a number of different depositional environments. Intriguingly, these clay minerals, hereafter referred to simply as 'clays', occur predominantly in terrains that are Noachian (>3.6 Ga) in age [Bibring et al., 2006]. The presence and apparent spatial and temporal distribution of these clays has been used to infer that early Mars was characterized by circum-neutral pH, low salinity, and possibly habitable conditions [Ehlmann et al., 2011]. More recently, *in situ* observations of clay-bearing mudstones in Gale Crater by the Curiosity rover are also supportive of a habitable environment, possibly during the Hesperian [Grotzinger et al., 2014; 2015; Vaniman et al., 2014; Bristow et al., 2015].

In contrast, sulfate detections on Mars typically occur in younger Hesperian terrains and may be indicative of a decreased hydrological cycle [Bibring et al., 2006]. Decreased water availability, coupled with increasing salinity, may indicate near-surface conditions inhospitable to most life [e.g., Tosca et al., 2008a]. Though many sulfate salts (e.g., Ca, Na, and Mg-sulfates) can form under a wide range of pH

151 conditions, it is worth noting that Al^{3+} and Fe^{3+}-sulfates are indicative of low-pH
152 fluids. As such, understanding the distribution and geologic setting of these minerals
153 on Mars has important implications for deciphering ancient aqueous chemistry,
154 whether it be indicative of surface waters, groundwater, or diagenetic fluids.
155
156 Jarosite, a ferric sulfate that forms under acidic conditions and that was first
157 detected on Mars by the Opportunity Rover in Meridiani Planum [Squyres et al.,
158 2004], has received considerable attention in this context. Integrated payload
159 observations by the rover reveal that jarosite is likely associated with Mg and Ca-
160 sulfates at this location, all of which occur in eolian sandstones that have been
161 interpreted as reworked dune and playa sediments [Grotzinger et al., 2005]. The
162 Curiosity rover has also detected small amounts of jarosite in clay-bearing
163 laminated mudstones in Gale Crater [Cavanagh et al., 2015], though the origin of this
164 phase (e.g., detrital or authigenic) in these deposits is not yet well constrained.
165
166 Orbital observations of jarosite and other possible ferric sulfates have also
167 been reported in the Mawrth Vallis, Aram Chaos, Noctis Labyrinthus, and Valles
168 Marineris regions of Mars [Bibring et al., 2007; Milliken et al., 2008; Farrand et al.,
169 2009; Metz et al., 2009; Lichtenberg et al., 2010; Weitz et al., 2010; Thollot et al.,
170 2011; Noe Dobrea et al., 2011]. Of the Valles Marineris detections, possible
171 submarine fan deposits in Melas Chasma and strata exposed on the surrounding
172 plains are notable in that ferric sulfates are found in proximity to other hydrated
173 minerals such as opaline silica, providing additional constraints on local aqueous

174 geochemistry [Milliken et al., 2008; Metz et al., 2009]. These rover- and orbiter-
175 based observations indicate ferric sulfates may be common alteration or diagenetic
176 phases on Mars, as discussed by Burns [1988; 1993], and understanding their
177 occurrence can provide insight into local, regional, or global redox conditions.
178
179 *2.2 CRISM Observations of the Spectral 'Doublet'*
180
181 CRISM spectra of martian deposits that exhibit the 'doublet' feature
182 mentioned above are characterized by absorption maxima (reflectance minima)
183 occurring at wavelengths of 2.205-2.218 and 2.265-2.278 μm. These spectral
184 features have been noted previously in a number of CRISM-based studies,
185 particularly for deposits within Valles Marineris, and in some of these studies the
186 material has been referred to as a hydrated silicate [e.g., Roach et al., 2010].
187 However, many minerals, including gypsum, jarosite, nontronite, and silica, exhibit
188 absorptions in this wavelength range, and it is possible that the spectral doublet
189 represents a mixture of two or more hydrated minerals (Figure 1). The main
190 doublet feature is consistent with vibrational absorptions due to the presence of
191 cation-OH bonds, although the position and shape of absorptions within the feature
192 lead to ambiguity in determining the specific cation(s). The shorter wavelength
193 absorption (~2.21 μm) may be consistent with Si- or Al-OH bonds, whereas the
194 longer wavelength feature (~2.27 μm) may be indicative of Fe- or Mg-OH bonds.
195 However, spectra of H_2O-bearing Ca-sulfates such as gypsum also exhibit

196 absorptions in this wavelength region, despite the lack of structural Si, Al, Fe, Mg, or
197 OH.
198
199 In addition, CRISM spectra that exhibit the doublet feature also exhibit an
200 absorption at ~1.9 μm due to the combination stretch+bend vibration mode of H_2O.
201 A similar doublet absorption has also been observed in laboratory spectra of poorly
202 crystalline Fe-silicate and sulfate mixtures [Tosca et al., 2008b] as well as acid-
203 leached Fe-smectite [Madejova et al., 2009], suggesting the spectral signature may
204 also be consistent with poorly crystalline or amorphous phases. Therefore, while it
205 is likely that the spectral doublet feature is indicative of OH and/or H_2O-bearing
206 phases, the specific mineral assignments remain ambiguous.
207
208 Roach et al. [2010] proposed four hypotheses to explain the doublet
209 material: (1) a mixture of sulfates (in particular, sulfates structurally similar to
210 gypsum and jarosite), (2) a mixture of opaline silica and Fe/Mg-smectite, (3) an Al-
211 OH phase mixed with Fe/Mg-smectite and/or jarosite, and (4) acid-leached Fe/Mg-
212 smectite or neoformation of poorly crystalline clays. Subsequent study by Weitz et
213 al. [2014] supported the latter two hypotheses based on an analysis of CRISM
214 spectra for the Melas Chasma region, demonstrating that the spectral doublet is
215 associated with "light-toned draping deposits" (termed LD in Weitz et al., 2014) that
216 locally form some of the highest stratigraphic units. These LD deposits extend
217 through portions of Melas Chasma and drape over pre-existing topography,
218 suggesting an airfall origin. Weitz et al. [2014] interpreted this LD unit to have been

219 deposited after the Late Hesperian valleys that incise the walls of the chasma, but
220 stratigraphic position alone cannot be used to determine whether the hydrated
221 phase(s) associated with the spectral doublet in this unit represent transported
222 sediments or authigenic products.
223
224 Roach et al. [2010] described a similar thin light-toned unit in Ius Chasma
225 that drapes pre-existing topography, but the stratigraphic and possible genetic
226 relationships between this unit and those in Melas have not yet been established.
227 Roach et al. [2010] interpreted the light-toned unit to have been emplaced on top of
228 Fe/Mg-smectite and sulfate-bearing strata either during or after a period of acidic
229 aqueous alteration when sulfates formed from evaporating brines. Another study by
230 Weitz et al. [2011], of Noctis Labrynthis, identified the doublet material in a ~20 m-
231 thick massive light-toned unit that outcrops near the top of a stratified light-toned
232 deposit [see Weitz et al., 2011 Figure 2]. It was suggested that this deposit was also
233 formed under acidic conditions, and the doublet-bearing unit was interpreted to
234 pre-date deposition of Fe/Mg- smectite and sulfates in the same region [Weitz et al.,
235 2011]. Although the doublet-bearing materials in Valles Marineris are often
236 associated with units that drape pre-existing topography, including the canyon
237 wallrock, Metz et al. [2010] provided evidence for deformation features in some of
238 the deposits, suggesting they may have originated higher up the canyon walls than
239 indicated by their current topographic position. Finally, CRISM data for Mawrth
240 Vallis also show evidence for doublet-bearing materials in the vicinity of Fe/Mg-
241 smectites and Al-phyllosilicates [Noe Dobrea et al., 2011; Bishop et al., 2013].

242

243 To summarize, doublet-bearing units are present in stratigraphic sections
244 that contain hydrated minerals suggestive of complicated and extended periods of
245 water-rock interaction and/or sediment transport. Fe/Mg-smectites and sulfates are
246 often found in nearby units and in most cases these occur in strata emplaced prior
247 to the doublet-bearing units. An exception is Noctis Labrynthis, where the doublet
248 material occurs in a unit that lies stratigraphically below an Fe/Mg smectite-bearing
249 outcrop.

250

251 We note that jarosite, which typically forms under conditions of pH<4, is also
252 identified in several of the regions that also exhibit the spectral doublet [Milliken et
253 al., 2008, Metz et al., 2009, Noe Dobrea et al., 2011]. Although the jarosite deposits
254 are not necessarily in rocks that are stratigraphically adjacent to the doublet
255 materials, the presence of this mineral in these regions may provide insight into
256 local aqueous geochemistry. Jarosite deposits on Mars may have formed where
257 acidic sulfate-bearing water ponded and subsequently evaporated [Tosca and
258 McLennan, 2006], though it is also possible for jarosite to form through chemical
259 weathering of basalt [e.g., Madden et al., 2004]. Alternatively, acidic conditions that
260 lead to jarosite formation may be induced by local or regional oxidation of Fe^{2+}-
261 bearing fluids, possibly via the emergence of groundwater and interaction with the
262 oxidizing martian atmosphere [Hurowitz et al., 2009]. An important aspect of any of
263 these scenarios is that the presence of authigenic jarosite records information about
264 local pH as well as redox conditions.

265

266

267 *2.3 Overview of Field Region at Rio Tinto, Spain*

268 The headwaters of the Rio Tinto near Nerva, Spain are acidic (mean pH of
269 2.3) and rich in ferric iron and other heavy metals. Three terraces of the Rio Tinto
270 are exposed in the river valley with the youngest terrace closest in elevation to the
271 modern day channel and the intermediate and oldest terraces located
272 stratigraphically above it (see Figure 2). The youngest of these (called the lower or
273 young terrace) is Holocene in age (750-1500 years) and composed of poorly sorted
274 conglomerates overlain by cross-bedded sandstones. Both types of deposits are
275 consistent with formation by mass wasting and sediment accumulation in the active
276 channel, a process that also occurs in the modern river. The Pleistocene-aged (~35
277 Ky) intermediate terrace is exposed 100 m above the lower terrace and consists of
278 poorly sorted clasts of country rock within a goethite-bearing matrix; this terrace is
279 distinct from the other river terraces as it lacks the sedimentary facies
280 corresponding to channel and backwater deposits seen in both the young and old
281 terraces. Finally, the Late Pliocene-aged (2 My) upper or old terrace is exposed in a
282 ≥10m thick outcrop at Alto de la Mesa. The outcrop at Alto de la Mesa consists of a
283 lag conglomerate overlain by sandstones and iron oxide precipitates, reflecting
284 similar types of channel deposits as those seen in the lower terrace. Further
285 description of the terraces and radiometric age constraints are reported in
286 Fernández-Remolar and Knoll [2008].

287

The mineralogy of the modern river system and its terraces is dominated by ferric oxides and ferric sulfates. A number of previous studies have investigated variations in the mineralogical assemblages in the river terraces using X-ray diffraction (XRD), visible-near infrared (VIS-NIR) reflectance spectroscopy, and Raman spectroscopy [Fernández-Remolar et al., 2005; Roach et al., 2006; Chemtob et al., 2006; Sobron et al., 2009, 2014,]. The reader is directed to Fernández-Remolar et al. [2005] for a more thorough discussion on the mineralogy and mineral-forming processes of the Rio Tinto. Those authors found that seasonal precipitation of Ca- and Fe-sulfates occurs near the source region of the river, with the Fe-sulfates jarosite (in particular hydronium jarosite), schwertmannite, and copiapite making up much of the mineral assemblage, along with nanophase iron oxide and nanophase goethite. Only the most stable minerals (iron oxides, goethite, jarosite) survive through the wet season, during which meteoric water dissolves many of the precipitates and aids in cementation of the terrace deposits. Jarosite is less abundant and often absent in the older deposits, likely due to its long-term instability under wet conditions, and these units instead contain more stable Fe-oxides such as goethite and hematite. Therefore, the persistence of jarosite may indicate a low degree of water-rock interaction or low water-to-rock ratios since its precipitation. Country rock in this region is composed of quartz, chlorite, and pyrite, which act as a source of solutes for the precipitates as well as a source of detritus for the terrace conglomerates.

In addition to sulfates and Fe-oxides, phyllosilicates (2M1 illite, chlorite, kaolinite, and smectites) are also present throughout the Rio Tinto system and are thought to form by alteration of the volcanosedimentary bedrock near the source of the acidic river system [see Fernández-Remolar et al., 2011 for details]. At Rio Tinto, phyllosilicates typically accumulate at times of maximum waterflow during the wet season when deposition of detrital sediment is dominant over chemical sedimentation, but they can also be found in environments where conditions are outside those typical for clay formation, such as the low-pH source streams. The diversity and stability of these phyllosilicates depends on the hydrology, source rock composition and geochemical processes occurring in the river, all of which must be accounted for when interpreting the deposits [Fernández-Remolar et al., 2011]. Likewise, jarosite is neither stable nor formed in all of Rio Tinto's hydrogeochemical environments [Fernández-Remolar et al., 2005 and discussed below].

3. Methods

3.1 Hyperspectral Imaging Data

3.1.1 HyMap Data Analysis

For remote observations of Rio Tinto we used aerial HyMap scenes that covered the headwaters of the river, nearby mining activity, and urban areas. These data were acquired by Integrated Spectronics on Aug 14, 2004 and are the same as the fully processed and analyzed data used by Roach et al. [2006]. The reader is directed to that publication for a detailed description of how these data were

333 calibrated, atmospherically corrected, and processed. Briefly, HyMap is an aerial,
334 hyperspectral system with 126 channels covering a wavelength range of 0.45 to 2.5
335 μm at a spatial resolution of ~8m per pixel. Spectra from the processed images were
336 examined for individual pixels as well as spectral averages from multiple pixels that
337 correspond to larger regions of geologic or spectral interest, called regions of
338 interest (ROIs). Wavelengths from ~1.3 - 1.45 μm and ~1.8 - 2 μm were excluded
339 due to atmospheric absorptions. A principal component analysis (PCA) was carried
340 out for the data to reduce spectral variance and to highlight regions with similar
341 spectral properties (Figure 3). PCA is a purely mathematical procedure and does not
342 rely on a user's *a priori* knowledge of variability in a region; thus, it can be difficult
343 to attribute different features observed in PCA images to unique differences in
344 mineralogy. However, as a purely qualitative tool we found this method reliable for
345 highlighting regions in the HyMap scenes whose spectra exhibited the doublet
346 absorption feature (e.g., Figure 3).
347
348 *3.1.2 CRISM Data Analysis*
349
350 CRISM is a hyperspectral imaging system on NASA's Mars Reconnaissance
351 Orbiter that consists of several spectrometers. The "L" spectrometer covers near-
352 infrared wavelengths from 1.0 to 3.9 μm using 431 channels, has a spectral
353 resolution of ~6.55nm per channel, and a maximum spatial resolution of ~15-19 m
354 per pixel [Murchie et al., 2007]. The highest spatial-spectral resolution images are
355 Full Resolution Targeted (FRT) observations, and for this study we analyzed three of

these images in detail from the western Valles Marineris region near Melas and Ius Chasma (see Figure 4, Figure 9). A full description of CRISM image processing methods is provided in the supplemental material.

The variability in the doublet absorption feature was studied in detail by handpicking spectra from geologic units and ROIs that exhibited these spectral features. The resulting spectra commonly represent 3x3 or 5x5 pixel averages. Each spectrum was fit with an upper convex hull to define the spectral continuum over the ~2.1 to 2.35 μm wavelength range. The original spectra were then divided by these continuum fits to produce continuum-removed spectra. This step isolates the wavelength region where the doublet occurs and is necessary to compare band depths between spectra [Clark and Roush, 1984]. Band depth is defined as $1-[R_b(\lambda)/R_c(\lambda)]$, where R_b represents the observed reflectance value at wavelength λ and R_c represents the calculated reflectance of the spectral continuum fit at the same wavelength. Band depth maps were created for each CRISM image to provide a more in-depth analysis of the spatial distribution of the spectral doublet feature.

Gaussian curves were also fit to the continuum-removed doublet absorptions and the resulting Gaussian amplitudes and center positions were mapped for each CRISM image. Gaussian modeling of absorptions is commonly used for remote sensing data to assess band strength in the presence of noise or to remove the influence of adjacent or partially overlapping absorption features on the absorption of interest [Clark and Roush, 1984; Sunshine and Pieters, 1993]. Noise in the CRISM

images, for instance, may introduce apparent changes in band position/strength if these calculations are based on the observed absolute reflectance values on a pixel-by-pixel basis. This can introduce uncertainties in the band depth maps, which we attempt to mitigate by examining the amplitudes and positions of Gaussian fits.

To determine the background noise in an image prior to Gaussian fitting, a histogram of the standard deviations within each image was examined for a flat, absorption-free portion of the spectrum (1.70-1.85 μm), an example of which is presented in Figure 4. Here it is clear that the standard deviations in the ratio spectra are predominantly <0.005, thus any absorption feature (band depth) in the ratio spectra that is larger than this value is above the typical level of 'noise' in the CRISM image. Two CRISM ratio spectra exhibiting the doublet feature and their corresponding Gaussian fits are also presented in Figure 4, where it is clear that the doublet absorptions are much stronger than the typical channel-to-channel variation in reflectance. Pixels that exceed the 0.005 threshold are fit with two Gaussian curves, one for each absorption in the doublet (see example in Figure 4).

3.2 Field Measurements

Fieldwork was conducted at multiple locations in the vicinity of Rio Tinto, Spain in early May of 2014. Rock and/or soil specimens were collected and field spectra were acquired at each of five primary sites (Table 1). These locations included the modern streambed environment and two successively older terraces that have been affected to different degrees by diagenetic processes (Figure 2).

Previous studies have shown that the materials at these sites exhibit different mineral assemblages [Fernández-Remolar et al., 2005; Fernández-Remolar and Knoll, 2008], allowing us to examine whether spectral reflectance properties can be linked to post-depositional processes in these types of environments.

Samples collected were collected from the Rio Tinto source region (Anabel's Garden, Richi Spring, and Source Spring sites), a series of small streams with actively forming efflorescent and crust-forming precipitates (e.g. copiapite, jarosite, gypsum). A number of samples were also collected from an actively mined terrace directly above Anabel's Garden that showed evidence for the spectral doublet absorption in the airborne HyMap data. Another field site, Berrocal, is also located directly on the Rio Tinto approximately 20 km downriver from the mining operations. At this location, there is a mix of detrital sediment and authigenic precipitates. We also examined older deposits at Barranco de los Locos, a site that is part of the Holocene-aged lower terrace in which the lower unit is a ferruginous conglomerate and is overlain by sandstone [Fernández-Remolar et al., 2005]. Finally, for comparison to the modern environment we examined an older (early Quaternary) terrace exposed at Alto de la Mesa. Detailed descriptions of these sites, their ages, and local geology can be found in previous publications [e.g., Fernández-Remolar et al., 2005; Fernández-Remolar and Knoll, 2008; and references therein].

A portable VIS-NIR spectrometer (ASD FieldSpec 3®) was used to acquire reflectance spectra *in situ* from 0.35 to 2.5 μm. Reflectance spectra were acquired

425 for a variety of materials passively (relying on ambient sunlight) and/or actively
426 (relying on a contact probe with internal illumination). All measurements were
427 made using a Spectralon® panel as the reflectance standard. Passive measurements
428 that rely on solar illumination and reflectance are more directly analogous to
429 airborne data such as HyMap. A more detailed description of the ASD measurements
430 is provided in the supplemental material.
431
432 Rock and sediment samples were collected to capture the spectral diversity
433 of deposits at each location and were based in part on interesting absorption
434 features observed in the HyMap and field reflectance spectra (see Table 1 for full
435 list). To the extent possible, samples were collected at the different sites to be
436 representative of the mineralogy expected at HyMap and CRISM spatial scales (e.g.,
437 the dominant mineral assemblages at scales of ~8 - 18 m/pixel, respectively),
438 focusing on regions whose spectra exhibited evidence for compositional diversity.
439 Of specific interest were regions with spectral or field-based evidence for Fe-oxides,
440 Fe-sulfates, and clay minerals. A number of locations contained materials whose
441 reflectance spectra exhibited the doublet absorption feature described above, and a
442 variety of these materials were collected for detailed laboratory characterization.
443 Though many other samples and spectra were collected during the field campaign,
444 the samples, field measurements, and HyMap data whose spectra exhibit these
445 distinct doublet absorptions were chosen as the focus for the present study. A more
446 complete treatment of how field-based spectral observations and diversity at Rio

Tinto relate to aerial and orbital-scale observations is presented in Roach et al. [2006].

3.3 Laboratory Measurements

3.3.1 Sample Preparation

All laboratory analyses were conducted in the Department of Earth, Environmental and Planetary Sciences at Brown University. A number of small chips (~2.5 cm) were removed from each hand sample and a second portion of each was ground by hand in an agate mortar and pestle. The resulting powders were ground such that the material could pass through a <45 μm mesh sieve. Grinding and sieving serves the dual purpose of homogenizing the sample and reducing particle size-dependent absorption/scattering processes. Where possible, separate powders were prepared for different portions of a single sample to assess heterogeneity (e.g. rock varnish, dark or light components, areas with different degrees of weathering) and for comparison to the whole rock powders. Some hydrated mineral phases are expected to be unstable even over short time frames, and these are not included in our dataset.

3.3.2 Reflectance Measurements

Reflectance spectra of the hand samples, chips, and powders were measured in the laboratory using the same ASD FieldSpec 3 instrument over a wavelength range of 0.35 to 2.5 μm. The measurement spot size was adjusted to encompass the

entire sample in order to provide a better assessment of the bulk spectral properties of each hand, chip, and powder sample rather than averaging spectra of individual components. We note that the chips and powder samples were placed in ~10 mm diameter sample holders for measurement, thus the measurement spot size for these samples is equivalent.

All of the rock powders sieved to <45 μm were also measured with a Nicolet iS50 FTIR from 1.75 – 25 μm. The FTIR was equipped with a Praying Mantis diffuse reflectance attachment from Harrick Scientific and diffuse gold from Labsphere was used as a reflectance standard. These measurements used a KBr beamsplitter and DTGS detector, and each final spectrum was an average of 50 scans. Absolute reflectance values from the FTIR are highly dependent on any slight differences in height between the sample and gold standard, thus all FTIR spectra were scaled to match the ASD values at 1.7μm. These spliced spectra provide full VIS-NIR-mid-IR wavelength coverage, and because all samples were measured under identical conditions, the observed relative differences between samples are reliable.

All reflectance spectra (field and lab) were processed using the same methods, and continuum-removed spectra and band depths were calculated using the same procedures as described above for the CRISM data (i.e., an upper convex hull method was used to define the continuum slope). We analyzed the continuum-removed spectra using Matlab to find the local minima (which is equivalent to the maximum band depth) within the ~2.1 – 2.35 μm wavelength region. If the

493 continuum-removed spectrum is determined to exhibit absorptions near ~2.2 μm
494 and ~2.26 μm, then this so-called doublet feature is further analyzed to determine
495 the total width, center position, and depth of the individual absorptions.
496
497 *3.2.3 X-ray Diffraction Measurements*
498
499 The <45μm sieved powders were measured with a Bruker D2 Phaser XRD
500 system (see supplemental material for details) to determine qualitative and
501 quantitative mineralogy. Samples whose corresponding reflectance spectra
502 exhibited the 2.2 μm doublet (n = 8) were studied in detail, as were a subset of
503 samples from multiple locations whose spectra did not exhibit the doublet (n = 3) in
504 order to test our hypothesis that a distinct mineral assemblage gives rise to the
505 doublet feature (Table 2). Powder diffraction patterns were typically acquired over
506 a range of 2-90° 2θ, 0.02˚ step size, with a total integration time of up to ~12 hours
507 (6.5 s/step).
508
509 XRD patterns were analyzed with two programs, DIFFRAC.SUITE™ EVA for
510 full pattern phase identification and DIFFRAC.SUITE™ TOPAS for quantitative
511 Rietveld refinement, where the latter is similar to the method described in Bish and
512 Howard (1988). An overview of the mineralogy at Rio Tinto is provided in
513 Fernández-Remolar et al. [2005], which we used as a guideline for choosing
514 reasonable starting components for the qualitative mineral assessment. Modal
515 mineralogy estimated from Rietveld refinement relied on the structural and

516 instrumental parameters to model the XRD patterns. Structure files describing the
517 crystallographic structure of relevant minerals used in the refinement are listed in
518 the supplementary table.
519
520 These mineral structures were added and removed from the model
521 iteratively until a reasonable fit to the observed pattern was obtained. TOPAS
522 automatically normalizes the model results such that mineral abundances will
523 always add to 100%. The quality of the refinement is determined by the weighted
524 profile R-factor (R_{wp}), which considers the root mean square error (RMSE) for each
525 scaled intensity value (peak and background). Although a smaller R_{wp} generally
526 indicates a better model, it is possible to over fit the data with this method and
527 discretion is used to ensure the resulting model is geologically realistic. We also
528 calculated the areas for the muscovite 001 (~9° 2θ) and jarosite 101 (~15° 2θ)
529 peaks. Though this method does not provide quantitative estimates like the Rietveld
530 method, it does provide an independent estimate of how the relative abundances of
531 the two minerals vary between samples without the uncertainties associated with
532 modeling the full XRD pattern.
533
534 **4. Results**
535 **4.1 Overview of Rio Tinto Field Observations**
536 Previous work has shown that mineralogical and spectral differences exist
537 between the old and young terraces [Fernández-Remolar et al., 2005; Sobron et al.,
538 2014], and we observe congruous spectral differences in our samples from these

539 locations. Field spectra of samples from the source region exhibit absorptions
540 consistent with the presence of gypsum, jarosite, and copiapite (Figure 5). Hydrated
541 iron-bearing phases are also common in these field spectra, including absorptions
542 consistent with the presence of schwertmannite and copiapite, which are identified
543 in spectra from the Richi Spring and Source Spring locations. The field spectra from
544 Berrocal (not shown) have very similar identifying absorptions that are typical of
545 the precipitates, phyllosilicates and iron hydroxides found in the source region
546 spectra. Spectra exhibiting the doublet absorption are found in sand bar sediments
547 from Berrocal, representing rocks/sediments that have not been influenced by
548 mining activities.
549
550 Most of the Fe- and Ca-sulfate precipitates are absent at the young terrace
551 site, Barranco de los Locos. Jarosite, Al-phyllosilicate (muscovite/illite), and goethite
552 are the primary minerals identified in our field spectra at this location. VIS-NIR
553 spectra from the old terrace site, Alto de la Mesa, exhibit the lowest mineral
554 diversity and are dominated by iron oxides. Most spectra from Alto de la Mesa are
555 consistent with the presence of goethite, though some indicate the presence of
556 kaolinite or chlorite. Sulfate absorptions are not apparent in spectra of materials
557 from the old terrace, and the doublet feature is also not observed in these spectra.
558 However, spectra for a number of samples that were taken from a mine road terrace
559 above Anabel's garden display the doublet absorption. Other samples from this site
560 are spectrally consistent with goethite and hematite. Finally, samples from some of

561 the mining terraces are spectrally consistent with chlorite, kaolinite, and muscovite,
562 likely reflecting country rock components.
563
564 **4.2 Laboratory Measurements**
565 *4.2.1 X-ray Diffraction*
566
567 Based on an initial qualitative assessment of the XRD patterns and observed
568 spectral diversity, eleven samples were chosen for further quantitative Rietveld
569 refinement. Eight of the samples have spectra that exhibit the spectral doublet and
570 contain between 3 - 38% jarosite and 4 - 50% illite or muscovite (Table 2). The
571 other volumetrically important mineral in these samples is quartz, which does not
572 have absorptions at VIS-NIR wavelengths, so the samples are spectrally dominated
573 by Fe-sulfate and Al-bearing clay minerals. K-jarosite is a better fit in the Rietveld
574 refinement than either hydroniumjarosite or natrojarosite. Though the mineral
575 assemblage is largely the same, the relative proportion of jarosite and Al-clay is
576 quite variable between samples (Figure 6), and these values are presented in Table
577 2. Three samples that do not show evidence for the doublet feature in
578 corresponding reflectance spectra were also examined. The XRD patterns for these
579 samples are consistent with a mineral assemblage dominated by hematite, goethite,
580 kaolinite, chlorite and quartz, but no jarosite, in agreement with the findings of
581 Fernández-Remolar et al., [2005] for this locale (Table 2). One sample from the
582 young terrace, Barranco de los Locos sample RT23, is modeled to contain ~33%
583 jarosite and ~39% gypsum but no Al-clay (Table 2), and its reflectance spectrum is

584 dominated by gypsum at wavelengths >1.3 μm (Figure 5). In summary, the major
585 secondary phases in these samples are jarosite, illite or muscovite, and Fe-oxides
586 such as goethite and hematite. Although smectitic clays are an integral part of the
587 alteration mineral assemblages on Mars, the Rio Tinto samples examined for this
588 study show no clear evidence for the presence of smectitic clays.
589
590 *4.2.2 Reflectance Spectra*
591
592 As with the field spectra, the laboratory spectra indicate variations in
593 mineral assemblage with age. In samples from the modern streambeds (samples
594 from Anabel's Garden and Source Spring) gypsum is the primary mineral identified
595 in two samples (RT18, RT23), with jarosite also being present in RT23 (see Figure
596 5). Other samples from these sites have spectra with strong OH and H_2O bands at
597 ~1.4 and ~1.9 μm as well as absorptions consistent with copiapite, schwertmannite,
598 or possibly monohydrated sulfates (Figure 5). These hydrated samples were not
599 measured with XRD because these minerals change hydration states readily under
600 laboratory conditions, so these spectral mineral identifications cannot be confirmed.
601 However, other XRD studies of Rio Tinto samples have found evidence for a variety
602 of sulfates, including epsomite, copiapite, and coquimbite [Fernández-Remolar et al.,
603 2005], and it is likely that a range of hydrated sulfates are also present in our
604 samples.
605

606 The spectral shapes of samples from the young terrace are distinct from
607 those of Anabel's Garden and Source Spring, with the former having weaker
608 hydration absorptions and a strong spectral slope near 1 μm. In fact, the major
609 difference in spectra of all the young terrace samples lie in the region between 2.2
610 and 2.3 μm; spectra of some samples show a doublet in this region whereas others
611 have only an ~2.21 or 2.27 μm absorption. Samples collected from the old terrace
612 deposit are spectrally consistent with clays such as kaolinite and chlorite as well as
613 Fe-oxides such as hematite (Figure 5). Gossan samples all show spectral evidence of
614 goethite. As with the field spectra, lab measurements of the older samples typically
615 lack spectral evidence for sulfates and are instead indicative of Fe-oxides and/or
616 phyllosilicates. Samples from the mining terrace have spectra that exhibit the
617 spectral doublet or that are representative of the same types of minerals discussed
618 for the other sites, including chlorite and Fe-oxides (goethite and hematite).
619 However, given that the specific geologic context of these samples is unknown,
620 especially compared to the well-defined mineralogical and age progression of the
621 river terraces, it is difficult to comment on the processes that have affected this
622 group of samples.
623
624 To summarize thus far, laboratory spectra with the doublet absorption
625 correspond to samples collected from the modern stream sites (Anabel's Garden,
626 Source Spring), the young terrace (Barranco de los Locos), and from a mining
627 terrace site near Anabel's Garden (Table 2). There are many minerals that have
628 spectral features near 2.26 μm, but we attribute the 2.26 μm feature in the doublet

629 to jarosite because of the combined presence of absorptions at wavelength positions
630 that are attributed to jarosite (1.48, 1.86, 1.9, 2.26 μm), as well as evidence from
631 XRD mineralogical analysis. The doublet feature is conspicuously absent in spectra
632 of samples collected at the old terrace, all of which lack jarosite. Reflectance spectra
633 of the <45 μm powders of samples exhibiting the doublet show strong, broad
634 electronic transition absorptions at wavelengths of ~1 μm due to the presence of
635 iron (Figure 6). There are also narrower vibrational absorption features at 1.4 and
636 1.48 μm due to OH, though the 1.48 μm feature is weak or absent in samples that
637 show a very strong 2.21 μm short wavelength band in the doublet feature. Likewise,
638 a broader absorption at ~1.9-1.95 μm due to OH/H_2O and a narrower absorption at
639 1.86 μm from OH/H_2O are also weaker in samples with a stronger ~2.21 μm
640 feature.. In contrast, the ~2.21 μm absorption in the doublet feature is related to the
641 presence of Al-phyllosilicates (illite or muscovite). A vibrational absorption near
642 2.35 μm is present in some samples and is also consistent with the presence of Al-
643 OH in illite or muscovite.
644
645 Spectra of rock chips and hand samples were also acquired and, in most
646 cases, the samples whose powder spectra exhibited the doublet feature also exhibit
647 the feature for these larger physical forms (see example for sample RT19 in Figure
648 7). However, sample RT10 is an exception in that a spectrum of the orange-colored
649 varnished face of the hand sample shows the doublet feature whereas the
650 unvarnished side of the hand sample, a chip, and the powder spectra are dominated
651 by the 2.21 μm feature (Figure 7). This indicates the varnish may be enriched in

652 jarosite, and although such coatings or varnishes may be only several micrometers
653 thick, they may contribute significantly to aerial and orbital spectral observations.
654
655 Only the bulk powder versions of the samples were measured using both
656 reflectance spectroscopy and XRD; thus, we compare only the powder spectra
657 directly with the mineralogy determined by XRD. There is a strong correlation
658 between the strength of the longer wavelength absorption in the doublet feature
659 and the abundance of jarosite for the samples examined here (Figure 8). There is
660 also a strong relationship between the relative band strengths and the relative
661 amounts of jarosite and Al-clay in the samples, as determined using either the
662 Rietveld modal estimates or the XRD peak area. The relationship between Al-clay
663 and the strength of the shorter wavelength absorption has a lower R^2 value than in
664 the other plots, but we suggest this is due to the size of the dataset, where a
665 relatively small amount of scatter (in this case one data point with anomalously high
666 estimated Al-clay wt.%) has a strong control on the fit. These observations indicate
667 that the doublet feature observed in spectra of some samples from Rio Tinto is
668 related to the mixing of Al-phyllosilicate (illite or muscovite) with jarosite, and that
669 the strengths of the absorptions within the doublet feature are directly related to
670 the relative proportion of these phases.
671
672 **4.3 HyMap and CRISM Observations**
673 *4.3.1 HyMap Results*
674

675 The HyMap PCA false-color map presented in Figure 3 highlights pixels
676 whose spectra exhibit the doublet feature in dark red. Absorption maxima
677 (reflectance minima) for these pixels occur at ~2.20-2.22 and 2.26-2.28, a range that
678 is broader than observed in Mars CRISM data and that could be a result of
679 differences in spectral resolution, since HyMap only has 6 bands in this wavelength
680 region compared to CRISM's 13 bands. The doublet feature is evident in HyMap
681 spectra corresponding to the Anabel's Garden location, where it is possible to track
682 changes in the relative strength of the absorptions across a ~500 m transect in the
683 HyMap image (Figure 3). The feature is also present in numerous pixels
684 corresponding to mining terraces, although it was not possible to independently
685 examine most of these locations during the field study. Bedrock, detritus, and soil at
686 the young, intermediate, and old terrace sites discussed above are not always
687 apparent in the HyMap data due to the presence of vegetation. However, chlorite,
688 kaolinite, gypsum, and Al-clay are identifiable in the HyMap spectra, and Roach et al.
689 [2006] provide a thorough analysis of iron oxides and hydrated or hydroxylated
690 iron-sulfates in these airborne data. In this study we have only relied on the HyMap
691 data to provide an airborne comparison (at lower spatial and spectral resolution) of
692 the doublet-bearing materials with the spectra acquired in the lab and *in situ* using
693 the ASD FieldSpec3. In this context, the HyMap data confirm that spectra of certain
694 surface materials exhibit the doublet feature even at a meters-per-pixel spatial scale
695 and lower spectral resolution, consistent with the higher spatial and spectral
696 resolution field and laboratory data.
697

698 *4.3.2 CRISM Results*

699

700 The spectral doublet feature is evident in a number of CRISM images in the
701 Valles Marineris, with particularly good examples in Melas and Ius Chasma [e.g.
702 Roach et al., 2010, Weitz et al., 2014]. Our Gaussian fit analysis of three of these
703 CRISM images show that the absorption band centers and relative strengths
704 (Gaussian amplitudes) associated with the doublet materials are only moderately
705 variable (Figure 9). The centers of the Gaussian fits for the three CRISM images and
706 the HyMap image are listed in Table 3. The typical 2σ deviation on the band
707 positions in the CRISM images is ~0.015 μm and the band centers fall near 2.2060
708 and 2.2682 μm on average. However, the wavelength position varies across the
709 spatial dimension of the CRISM detector (spectral smile) by ~0.010 μm, which may
710 explain much of the width of the histograms in Figure 9. To examine this effect we
711 analyzed a 50 x 50 pixel region restricted to the center of each image where the
712 spectral smile is minimal. Histograms for these subsets reveal a decrease in
713 standard deviation as well as a shift in mean band center in all three cases (Table 3,
714 Figure 4). The difference in band centers between the full image and the central
715 subset is statistically significant ($p < 0.05$) in every case.

716

717 Therefore, we conclude that the band centers of the doublet spectral feature
718 are relatively constant and occur at wavelengths of ~2.21 and ~2.265-2.270 μm. It
719 should be noted that Weitz et al. [2014] identified another spectral doublet
720 occurrence with a long wavelength absorption closer to ~2.28 μm, and the inclusion

721 of pixels with this feature in our analysis would create additional spread in the
722 histograms in Figure 9c. Given that we did not analyze each pixel in each image
723 individually, it is possible that this longer wavelength doublet is present, but it is
724 certainly not a dominant spectral signature, which is evident in the histograms and
725 investigation of spectra from individual pixels and ROIs.
726
727 While the wavelength positions of the two absorptions appear to be fixed,
728 their relative strengths are variable and are not directly correlated (Figure 9d).
729 Though this result is qualitatively similar to what is observed in field, lab and
730 HyMap spectra of materials from Rio Tinto, the range in relative amplitudes of the
731 two absorptions is typically much smaller in the CRISM data than for the terrestrial
732 examples. That is, spectra of some materials from Rio Tinto are clearly dominated
733 by the ~2.21 or the ~2.27 μm feature, with the other feature being very weak or
734 absent. In contrast, nearly all CRISM spectra for the regions examined here exhibit
735 both features and in many instances both features are of equal strength and, while
736 variability does exist, it is less intense than the variability in strengths observed in
737 the Rio Tinto spectra.
738
739 The relative band strengths, which is the Gaussian amplitude of the 2.21 μm
740 absorption divided by the amplitude of the 2.27 μm absorption, for the three CRISM
741 images is 1.1925±1.47 (2σ), 1.2714±1.35 (2σ), and 1.2207±1.28 (2σ). These
742 averages suggest that the band strength of the shorter wavelength absorption is
743 often slightly stronger than the longer wavelength absorption. However, the

744 standard deviation of the distribution is large enough that it is clear the two
745 absorptions do not co-vary. That is, the two absorptions that comprise the doublet
746 feature in CRISM spectra are independent of one another and thus represent two or
747 more distinct phases. Both tails of the distributions in Figure 9d are affected by
748 "bad" pixel values (typically a spike in the value for a single CRISM channel in one
749 column of the image that will influence the Gaussian fits). This is particularly
750 obvious as a bulge in the distribution as the Band 1/Band 2 amplitude ratio
751 approaches 0 (due to Band 1 amplitudes approaching 0) as well as by the long tail as
752 the Band 2 amplitude approaches 0, starting at a band amplitude ratio of ~3.
753 However, other than the extreme tails of the distributions (which represent a
754 relatively small number of pixels), these pixels play a minimal role in the overall
755 distributions of the band amplitude ratios.
756
757 **4.4 A Case Study: Doublet-Bearing Materials in Ius Chasma, Mars**
758
759 This study is focused on the spectral characteristics of materials found on
760 Mars and how they relate to those in Rio Tinto as seen in field, airborne, and lab
761 data, with the goal of assessing whether or not the latter may be appropriate
762 mineralogical analogs. However, to fully understand the processes and
763 environmental conditions associated with the deposits on Mars, and whether or not
764 Rio Tinto is an appropriate process analog, it will be necessary to conduct detailed
765 mapping studies that place the martian examples in their proper geologic context.
766 We conducted a small-scale examination of MRO HiRISE and CTX images of the

767 doublet-bearing materials in Valles Marineris to get a sense of the stratigraphic
768 position of these deposits with respect to surrounding strata.
769
770 As discussed by Roach et al. [2010], some occurrences of the materials with
771 the doublet absorption are in proximity to Fe/Mg clay-bearing strata. However, in
772 many cases the contacts between units are obscured and bedding is not apparent,
773 making it difficult to determine the relative stratigraphic position of these units.
774 Despite these complications, it is clear that the doublet absorptions are commonly
775 associated with light-toned units that drape pre-existing topography and span a
776 range in elevation (e.g., Figure 10a) or as deposits within the topographically lower
777 portions of the chasma (e.g., Figure 10b). In some locations the doublet unit
778 surrounds the clay-bearing units, whereas in others the clay-bearing unit is located
779 higher up the canyon wall. The doublet material also occurs as matrix in
780 megabreccia deposits [Roach et al., 2010], an example of which can be seen in
781 CRISM image FRT0000A396 in Figure 9. We now discuss a case study for one region
782 in Ius Chasma where several doublet-bearing units are in proximity to Mg/Fe clay-
783 bearing strata, focusing on the relative stratigraphic position of these units in order
784 to assess the relationship between the observed mineral assemblages in a more
785 detailed geologic context.
786
787 The relative strength of absorptions in the doublet feature were mapped for
788 several CRISM observations in Ius Chasma and overlain on HiRISE and CTX images
789 (Figure 11). This map reveals both the full extent of the doublet-bearing units and

allows for further discrimination of spectral properties within and between the different units. Each colored pixel meets the criteria of having band depth > 0.005 at both 2.205 and 2.269 μm. Where the ratio of band depths (BD 2.205/2.269 μm) is small, we interpret the unit to be enriched in the ~2.27 μm phase, and a higher ratio represents the opposite, in a strictly relative sense. In some locations (Figure 11c) there is a full transition between these cases within a single unit. In this example, the unit is heavily brecciated and lacks clear stratification. This example fits within a larger regional trend where the doublet-bearing units with the strongest ~2.27 μm absorption are in the south, and seemingly higher up the walls of the chasm, which then transitions to a topographically lower region where the doublet has an absorption with two bands of equal strength, and finally to the north where the ~2.21 μm absorption becomes stronger in the floor units (see the red-to-green-to-blue northerly progression in Figure 11b). In this example it is clear that the doublet-bearing unit is quite heterogeneous with regard to the strength of the two absorptions, suggesting the relative abundances of the phases responsible for these absorptions are also highly variable within this single geologic unit.

A second example reveals changes in composition that are consistent with geomorphologic changes and that conform to geologic contacts. Three doublet-bearing units ("bright", "light", and "moderate"-toned) and a darker, stratified, Mg/Fe clay-rich unit are shown in Figure 11d, with close-up HiRISE views of the contacts between these units presented in Figure 12. The Mg/Fe clay unit has tilted strata (dipping approximately north/northwest, see Figure 12b) and spectra for

these units do not meet the criteria for being "doublet bearing" (with the exception of a few pixels that have high band ratios and therefore higher amounts of the ~2.21 μm component). These stratified Mg/Fe clay units are superposed by a light-toned doublet-bearing unit. The significant difference in bedding geometry and the sharp nature of the contact suggests there is an angular unconformity between these units, with the clay strata predating the doublet-bearing unit (Figure 12b). This light-toned doublet unit has a relative band strength ratio of ~1, meaning the absorptions within the doublet are of equal strength (however, this does not necessarily imply that there must be equal amounts of each component). Overlying this unit is a second doublet-bearing unit that is moderate in tone but that exhibits similar morphological characteristics as the light-toned unit (Figure 12c). At full HiRISE resolution it is apparent that both the light and moderate-toned units are stratified. The moderate-toned unit has a band strength ratio between 1.2 and 1.8, indicating the shorter wavelength (~2.21 μm) absorption is stronger.

The third unit in this region corresponds to pixels with band ratios <0.9, consistent with it being enriched in the longer wavelength (~2.27 μm) component relative to the other doublet-bearing units in this location. This unit is the brightest in grayscale HiRISE and CTX images and is overlain by the light-toned unit (Figure 12d). In this location there is no direct contact between the dark-toned Mg/Fe clay strata and this bright unit, thus the relative stratigraphic order cannot be determined. However, in nearby locations it appears that this bright-toned unit that is characterized by a stronger ~2.27 μm band is also stratigraphically above the

836 Mg/Fe clay-bearing unit, though these individual outcrops are too small to identify
837 compositionally with CRISM. Therefore, the apparent increasing stratigraphic order
838 is: Mg/Fe clay strata – (angular unconformity) – bright unit – light unit – moderate
839 unit. The associated mineralogy above the unconformity appears to decrease in the
840 longer wavelength (~2.27 μm) component and increase in the shorter wavelength
841 (~2.21 μm) component upsection, at least in a relative sense.
842
843 Together, these two examples indicate that the relationships between the
844 minerals responsible for the doublet feature and the local stratigraphy are diverse.
845 In the first example there appears to be spectral variation, and thus relative changes
846 in mineral abundance, within a single geologic unit. In the second case the dominant
847 spectral variations appear to conform to stratigraphic boundaries, indicating
848 differences in relative mineral abundance as a function of geologic unit and
849 stratigraphic position.
850
851
852 **5. Discussion**
853 *5.1 Mineralogy*
854
855 The CRISM spectral doublet feature is similar to features observed in
856 airborne, field, and laboratory spectra of materials in and around Rio Tinto, Spain.
857 As discussed above, XRD analysis of select Rio Tinto samples demonstrates that this
858 spectral doublet arises from a mixture of Al-bearing phyllosilicates and jarosite. By

analogy, CRISM spectra exhibiting the doublet feature may also arise from a mixture of Al-phyllosilicates and jarosite, one of the possibilities discussed by Roach et al. [2010] and Weitz et al. [2014]. This interpretation is supported because (1) the two absorptions that comprise the doublet feature vary independently, suggesting at least two phases are present, (2) the absorption features within the martian doublet examples occur at the same wavelength positions as observed in the Rio Tinto spectra and are consistent with Al-OH and Fe-OH vibrations, and (3) the doublet-bearing material occurs on Mars in the vicinity of other phyllosilicate and/or jarosite-bearing deposits. Therefore, we conclude that Al-phyllosilicate-jarosite mixtures in the Rio Tinto may serve as *spectral* analogs for the doublet materials found in the Valles Marineris and elsewhere on Mars. However, whether or not the Rio Tinto deposits may also serve as *process* analogs warrants further study, as discussed below.

Other suggestions for the doublet feature have included opaline silica and clay, mixtures of sulfates (e.g. gypsum and jarosite), and poorly crystalline Fe-SiO_4-bearing phases. Reflectance spectra of opaline silica do exhibit a broad absorption feature from 2.2-2.26 μm [Milliken et al., 2008], but it has been noted that this feature is typically too broad to match the doublet even when mixed with Fe-rich clay such as nontronite [Weitz et al., 2014]. One of our Rio Tinto hand samples, RT23, provides a natural example of an intimate mixture of jarosite and gypsum in which there are similar proportions of both phases and no phyllosilicates (Figure 5). The reflectance spectrum of this sample is clearly dominated by the H_2O absorptions

characteristic of gypsum and an absorption near 2.2-2.3 μm that is wider than observed for the typical doublet feature. In addition, although gypsum exhibits very narrow absorption features near ~2.22 and ~2.27 μm, these are rather weak and they are superposed on the much broader and stronger feature that spans the ~2.08-2.3 μm region (see gypsum spectrum in Figure 1). By contrast, the absorptions in the doublet feature do not appear to be superposed on any broader feature and each appears to be much stronger and more clearly defined than the narrow features observed at similar wavelengths in gypsum. In summary, it does not seem possible to recreate the shape of the doublet feature through a combination of only gypsum and jarosite, thus we consider the doublet feature to be most consistent with a mixture of an Al-phyllosilicate and jarosite.

In our Rio Tinto samples the Al-phyllosilicate is dominated by illite or muscovite and is likely to be detrital, sourced from the surrounding country rock. In contrast, the jarosite, which in some samples occurs as a coating, is authigenic and a natural product of the Fe- and S-rich, oxidizing, acidic conditions that characterize the Rio Tinto system. The decrease in jarosite with progression in age suggests it is not stable over geologic time in the continued presence of water, particularly for circum-neutral and higher pH fluids. Indeed, we observe the doublet feature only in spectra that contain jarosite, which are primarily associated with the youngest deposits such as those at Anabel's Garden and at the Source Spring. It is notable that in our Rio Tinto samples the spectral doublet feature can be directly attributed to relatively well-crystalline phases as there is no clear spectral or XRD evidence for

905 hydroxylated poorly crystalline phases that may result from the acidic leaching of
906 clay minerals. This is not to say that such processes do not occur in these locations,
907 but rather to note that the presence of acid-leached clays or hydrated poorly
908 crystalline precipitates are not required to explain the presence of the spectral
909 doublet feature in the samples examined here.
910
911 The same may not be true of the doublet-bearing materials on Mars. There,
912 acidic leaching of basalt and/or pre-existing smectitic clays may be an important
913 process for forming alteration minerals, including some sulfates such as jarosite
914 [e.g., Tosca et al., 2004; Golden et al., 2005]. As noted above, acid-leaching of clays
915 has also been invoked to explain the presence of the spectral doublet feature on
916 Mars [Tosca et al., 2008b; Roach et al., 2010; Noe Dobrea et al., 2011; Weitz et al.,
917 2014], and the occurrence of jarosite in some locations is indicative of low-pH
918 conditions, at least at a local scale. It is possible to make a poorly crystalline Fe-SiO_4-
919 bearing material through the acid leaching of nontronite, and reflectance spectra of
920 such products can exhibit absorptions with band centers similar to those observed
921 in the doublet feature [Madejova et al., 2009; Roach et al., 2010]. In this scenario, the
922 relative strengths of the absorptions may vary based on the degree of acid
923 alteration. However, spectra of residues from the acid leaching of nontronite may be
924 more consistent with Si-rich, opaline-like materials, and in these cases the full width
925 of the resulting doublet feature is slightly wider than is observed in the martian
926 examples [Tosca et al., 2008b; Altheide et al., 2010].
927

928 As a different example, reflectance spectra of Fe/Mg smectite-rich altered
929 basalts from Mauna Kea, Hawaii that have undergone acid leaching exhibit a doublet
930 feature that is thought to arise from the presence of jarosite and hallyosite [Graff et
931 al., 2012]. In this instance the spectral doublet feature is the result of two distinct
932 (presumably authigenic) mineral phases likely produced by
933 dissolution/transformation of pre-existing phases and not associated with a poorly-
934 crystalline leached clay residue. The spectral characteristics of halloysite-jarosite
935 mixtures, as presented in Graff et al. [2012], are more consistent with the doublet
936 characteristics observed on Mars than are the spectral characteristics of a Si-rich
937 leached clay residue. Spectra of the latter tend to exhibit absorptions in the ~2.2-2.3
938 μm region that span a slightly broader wavelength range than the martian examples
939 and for which the individual absorptions are not as narrow or well-defined as the
940 martian examples. Halloysite and kaolinite are spectrally similar in the ~2.2-2.3 μm
941 region, thus halloysite-jarosite, kaolinite-jarosite, and montmorillonite/illite-
942 jarosite mixtures could all be consistent with the martian doublet materials.
943
944 Perhaps akin to the observations by Graff et al. [2012], laboratory
945 experiments by Tosca et al. [2008b] indicate that dissolution of basalt and addition
946 of sulfur could lead to fluids that form precipitates under oxidizing conditions
947 whose spectra also exhibit a doublet between 2.2 and 2.3 μm [see example spectrum
948 in Roach et al., 2010]. Though some of the precipitates generated during these
949 experiments were X-ray amorphous, others exhibited XRD patterns consistent with
950 neoformation of jarosite, Fe-oxides, and opaline silica [Tosca et al., 2008b]. VIS-NIR

951 reflectance spectra of these precipitates were also consistent with the presence of
952 opaline silica, minor jarosite, and an Al-OH bearing phase, though the mineralogical
953 host(s) of observed Al-OH bands at ~2.21 μm was not directly evident in the XRD
954 data and it/they may be below the XRD detection limit.
955
956
957 *5.2 Formation Processes: Detrital and Authigenic*
958
959 From a process point of view the distinction between the scenarios described
960 above may be somewhat semantic. The important point is simply the recognition
961 that dissolution and alteration of basaltic materials on Mars, including cases where
962 clay minerals may already be present, can lead to fluids capable of forming jarosite
963 and Al-rich phyllosilicates. However, co-occurrence in the martian deposits does not
964 necessarily imply that both jarosite and Al-phyllosilicates were formed at the same
965 time, under the same conditions, or even in the same region. Either mineral could be
966 detrital or authigenic in the doublet-bearing units, and detailed geologic context in
967 conjunction with an assessment of the full mineral assemblage is needed to assess
968 which scenario is most likely.
969
970 Given that halloysite, kaolinite, muscovite/illite, and montmorillonite all
971 exhibit an absorption feature at ~2.21 μm and that all have been identified on Mars
972 from CRISM data [Ehlmann et al., 2009], it may be difficult to unambiguously
973 determine which Al-bearing phyllosilicate is present in these purported mixtures

974 using VIS-NIR reflectance spectroscopy alone. There is evidence in some of the
975 martian spectra that the doublet feature may exhibit a shoulder on the short
976 wavelength side of the ~2.21 μm absorption, indicating a weak and narrow
977 absorption may be present in the ~2.15-2.21 μm region. If true, this could be more
978 consistent with the presence of kaolinite or halloysite as the Al-bearing
979 phyllosilicate as opposed to illite or muscovite or montmorillonite. The presence of
980 jarosite would indicate low-pH conditions (at least locally), and previous studies
981 have noted that kaolin minerals can be formed under acidic conditions [e.g., Fialips
982 et al., 2000]. On Mars, oxidation of fluids enriched in ferrous iron could lead to local
983 (and transient) acidification, which could promote jarosite formation if sulfides are
984 present or if sulfate is present in solution [e.g., Hurowitz et al., 2009, 2010].
985
986 The processes described above indicate the possibility that both the Al-
987 phyllosilicates and jarosite are authigenic and thus indicative of local aqueous
988 geochemical conditions. Though some Al-phyllosilicates can form under moderate
989 to low-pH conditions, particularly kaolinite, an alternative possibility is that the Al-
990 phyllosilicates in the martian doublet materials are detrital. In this scenario the
991 jarosite would be indicative of local aqueous conditions and the phyllosilicates
992 would reflect eolian or aqueous sediment transport processes. If true, the doublet-
993 bearing units in Valles Marineris may be similar to Rio Tinto in terms of mineralogy
994 *and* process, in which case the relative proportions of Al-phyllosilicate and jarosite
995 in a given deposit could reflect the relative contributions of sediment input and
996 mineral precipitation, respectively. Recent experimental work by Dixon et al. [2015]

997 demonstrated that jarosite dissolution is not strongly dependent on hydrologic
998 conditions and that 1 mm jarosite particles are unlikely to survive for more than 10^4
999 - 10^5 years even at low flow rates (<0.01 L hr^{-1}). Therefore, while it is possible that
1000 the jarosite on Mars may be detrital, this is unlikely to be the case for long-lived
1001 fluvial transport systems, similar to the lack of jarosite observed in the older
1002 deposits at Rio Tinto. That stated, because we cannot constrain the particle size of
1003 the jarosite we cannot rule out eolian transport for this component.
1004
1005 A detailed 'source to sink' and stratigraphic study of the geologic setting of
1006 each of the doublet bearing units on Mars is needed to help determine which ones
1007 may represent diagenetic/authigenic phases (do observed mineral boundaries cut
1008 across the stratigraphy?) versus those that may be detrital (do variations in
1009 mineralogy conform to stratigraphic boundaries?), which is beyond the scope of the
1010 current study. However, given the diversity in morphologic properties of the
1011 doublet-bearing units within Valles Marineris and the results of the case study
1012 described above, it is likely that multiple formation processes are responsible even
1013 though the spectral signatures are similar.
1014
1015 The massive brecciated deposit in Ius Chasma that shows a relative
1016 transition from more jarosite to more Al-phyllosilicate within a single geologic unit
1017 (first example in our case study, Figure 11c) could be evidence of *in situ* alteration.
1018 Similarly, the thin draping units such as the one shown in Figure 10a are difficult to
1019 explain by processes other than airfall deposition [e.g., Weitz et al., 2015], which

would suggest a relatively fine grain size and thus make the original sediment more susceptible to chemical alteration if it has not been welded. In this case, the draping unit may be an airfall dust or volcanic ash deposit, either of which could contain sulfur, that was later altered by water, possibly in the form of thins films from melting snow or ice. Atmospheric sources of sulfur (e.g., from volcanic emissions) could also contribute to authigenic sulfate formation. Regardless of the source, local differences in iron and/or sulfur content of the original sediment would lead to different authigenic mineral assemblages, such as different amounts of Al-phyllosilicate and jarosite [Michalski et al., 2013].

The second example in our case study of Ius Chasma , where Mg/Fe clay-bearing strata are unconformably overlain by layers have differing amounts of inferred jarosite and Al-phyllosilicate (Figures 11-12), may be more consistent with changes in sediment flux and/or source region. The stratigraphic order of these units indicates the large Fe/Mg clay unit pre-dates deposition of the units with the doublet feature. Indeed, there is no clear genetic relationship between the Mg/Fe clay unit and the doublet units, suggesting the latter are inconsistent with *in situ* alteration or leaching of the former. One possible interpretation is that the different proportions of the Al-phyllosilicate component, which correspond to distinct stratigraphic units, represent changes in sediment flux and or source region, perhaps where an increase in Al-phyllosilicate corresponds to a more highly weathered source region. Unlike the other example we presented for this region, the relative strength of the ~2.27 μm jarosite absorption also appears to conform to

1043 stratigraphic boundaries. This may indicate that the jarosite is also detrital, but an
1044 authigenic origin is possible as well since pore fluid flow or chemistry may be
1045 stratigraphically controlled.
1046
1047 If this sequence in Ius Chasma does in fact represent different relative
1048 amounts of authigenic jarosite and detrital Al-phyllosilicate, then we are potentially
1049 observing an upsection transition from precipitate (jarosite) dominated lithologies
1050 to ones dominated by clastic input. Such stratigraphic changes in mineralogy could
1051 be formed in a variety of environments, and without modal abundances for these
1052 minerals it is difficult to narrow the possible interpretations. However, possibilities
1053 include decreasing either the abundance of jarosite cement (which may or may not
1054 correspond to a change in absolute Al-phyllosilicate content), the availability of
1055 water, and/or Fe or S availability. Alternatively, a change in redox conditions, pH, or
1056 an increase in detrital input through time could also influence the relative
1057 proportions of jarosite and Al-phyllosilicate. Regardless, the observation that there
1058 are deposits suggestive of both *in situ* alteration and a combination of detrital influx
1059 of clay and precipitation of sulfate shows that multiple aqueous processes were
1060 likely responsible for formation of the doublet-bearing materials.
1061
1062 One of the most intriguing features of the doublet-bearing rocks at Rio Tinto
1063 is that the associated mineral assemblage is not preserved through geologic time in
1064 a terrestrial environment. Influx of fresh meteoritic water removes sulfates,
1065 including jarosite, and results in a net increase in ferric oxides, predominantly

goethite, through time [Elwood Madden et al., 2004; Golden et al., 2005]. The transition from young sulfate-rich streambed deposits to older ferric oxide-rich terraces takes place in less than a million years, which is in agreement with jarosite dissolution rates reported by Dixon et al. [2015]. That study also noted that jarosite dissolution rate is more likely to be controlled by mineral-surface reaction rates rather than hydrologic conditions. Assuming that the Valles Marineris deposits have been exposed on the surface since at least the Early Amazonian, the apparent persistence of jarosite indicates that interaction between the doublet materials and water (e.g., diagenetic overprinting) has been rather limited since the time of jarosite formation or deposition. Thus, while water is required for the formation of jarosite and phyllosilicates, and for some occurrences of the doublet materials water may have acted as a sediment transport agent, it is likely that post-deposition water-rock interaction has been significantly limited in these regions for hundreds of millions of years or longer.

In summary, it is important to keep in mind that the presence of a mineral or mineral assemblage in and of itself is not necessarily indicative of local aqueous geochemistry for a given outcrop or region. Mineral identifications, particularly those determined at spatial scales that are typical of orbital spectrometers (10s of meter per pixel or greater), must be placed in proper context to determine how they relate to geologic processes and environmental conditions. Specifically, it is critical to determine which minerals may be detrital versus authigenic (to the extent possible) and to assess the textural relationships between different mineral phases.

Do sulfates and/or phyllosilicates occur as cementing agents, vein fill, or clasts? For minerals that are indicative of specific chemical conditions, such as jarosite, does the abundance and/or presence of the phases require those conditions to be persistent or might they represent short-lived exceptions to very different background conditions? As it stands, addressing such questions typically requires detailed small-scale observations that are only achievable by rovers or humans, thus caution should be exercised when interpreting orbital observations in terms of specific geologic processes, particularly at small spatial scales.

6. Summary and Conclusions

An enigmatic doublet feature in reflectance spectra has been observed alongside hydrated mineral deposits in a number of regions on Mars. Previous studies have proposed that this spectral signature could arise from mixtures of hydrated minerals with known absorptions between 2.2 and 2.3 μm, including jarosite, gypsum, silica, Fe/Mg smectite, and Al-phyllosilicates. Possible spectral and mineralogical analogs from Rio Tinto are analyzed with a combination of laboratory, field, and aerial reflectance spectra and XRD analysis of the mineralogy and reveal that the doublet arises in rocks containing both illite or muscovite and jarosite. The martian doublet materials are also consistent with a mixture of Al-phyllosilicate and jarosite because (1) the wavelength positions of the martian doublet absorptions are similar to those observed in Rio Tinto data collected at lab, field, and airborne spatial scales, (2) the wavelength positions and widths of individual absorptions are

consistent with the presence of Al-OH and Fe-OH-bearing minerals, and (3) the strengths of the two absorptions in the doublet vary independently, implying the spectra represent a mixture of two or more components. Likely Al-phyllosilicates for the martian examples include montmorillonite, illite, and kaolinite/halloysite.

Two scenarios are proposed for the creation of these clay-sulfate assemblages on Mars in the context of a case study of deposits in Ius Chasma. In one example there are clear mineralogical changes (variations in relative proportions of jarosite and Al-phyllosilicate) within a single breccia unit. These deposits are consistent with *in situ* jarosite formation, possibly linked to diagenetic fluids. In a second example, observed changes in the relative proportions of the two minerals appear to follow stratigraphic boundaries, and in all cases the doublet-bearing units lie unconformably over Mg/Fe clay-bearing strata. A detrital origin for both phases cannot be ruled out in this case, but it is also plausible that the observed changes in mineralogy reflect changes in the relative contribution of precipitates (e.g., jarosite) versus detritus (e.g., Al-phyllosilicates) through time. Both detrital and authigenic origins are consistent for different doublet-bearing deposits in Ius Chasma, and the complexity of these deposits demonstrates the need for detailed mapping of each occurrence to decipher their likely geologic history. The results of such detailed mapping studies will ultimately provide the most insight into what these deposits record about aqueous activity, preservation potential, and water-rock-atmosphere interaction on Mars.

Acknowledgements

The authors would like to acknowledge the support of the NASA Astrobiology Institute (MIT team, award NNA13AA90A) for funding this work. We also thank John Mustard for providing the HyMap data and the NASA Reflectance Experiment LABoratory (RELAB) facility for providing some of the spectral data used in this study. Comments from an anonymous reviewer and Liz Rampe helped to improve this manuscript and their efforts are graciously acknowledged. All data used in this paper are available upon request through the corresponding author (Hannah_Kaplan@brown.edu).

References

Altheide, T.S., Chevrier, V.F., Noe Dobrea, E., 2010. Mineralogical characterization of acid weathered phyllosilicates with implications for secondary martian deposits. Geochimica et Cosmochimica Acta 74, 6232–6248. doi:10.1016/j.gca.2010.08.005

Arvidson, R.E., Ruff, S.W., Morris, R.V., Ming, D.W., Crumpler, L.S., Yen, A.S., Squyres, S.W., Sullivan, R.J., Bell, J.F., Cabrol, N.A., Clark, B.C., Farrand, W.H., Gellert, R., Greenberger, R., Grant, J.A., Guinness, E.A., Herkenhoff, K.E., Hurowitz, J.A., Johnson, J.R., Klingelhöfer, G., Lewis, K.W., Li, R., McCoy, T.J., Moersch, J., McSween, H.Y., Murchie, S.L., Schmidt, M., Schröder, C., Wang, A., Wiseman, S., Madsen, M.B., Goetz, W., McLennan, S.M., 2008. Spirit Mars Rover Mission to the Columbia Hills, Gusev Crater: Mission overview and selected results from the Cumberland Ridge to Home Plate. Journal of Geophysical Research 113. doi:10.1029/2008JE003183

Bibring, J.-P., 2006. Global Mineralogical and Aqueous Mars History Derived from OMEGA/Mars Express Data. Science 312, 400–404. doi:10.1126/science.1122659

Bibring, J.-P., Arvidson, R.E., Gendrin, A., Gondet, B., Langevin, Y., Le Mouelic, S., Mangold, N., Morris, R.V., Mustard, J.F., Poulet, F., Quantin, C., Sotin, C., 2007. Coupled Ferric Oxides and Sulfates on the Martian Surface. Science 317, 1206–1210. doi:10.1126/science.1144174

Bish, D.L., Howard, S.A., 1988. Quantitative phase analysis using the Rietveld method. Journal of Applied Crystallography 21, 86–91. doi:10.1107/S0021889887009415

Bishop, J.L., Loizeau, D., McKeown, N.K., Saper, L., Dyar, M.D., Des Marais, D.J., Parente, M., Murchie, S.L., 2013. What the ancient phyllosilicates at Mawrth Vallis can tell us about possible habitability on early Mars. Planetary and Space Science 86, 130–149. doi:10.1016/j.pss.2013.05.006

Bristow, T.F., Bish, D.L., Vaniman, D.T., Morris, R.V., Blake, D.F., Grotzinger, J.P., Rampe, E.B., Crisp, J.A., Achilles, C.N., Ming, D.W., Ehlmann, B.L., King, P.L., Bridges, J.C., Eigenbrode, J.L., Sumner, D.Y., Chipera, S.J., Moorokian, J.M., Treiman, A.H., Morrison, S.M., Downs, R.T., Farmer, J.D., Marais, D.D., Sarrazin, P., Floyd, M.M., Mischna, M.A., McAdam, A.C., 2015. The origin and implications of clay minerals from Yellowknife Bay, Gale crater, Mars. American Mineralogist 100, 824–836. doi:10.2138/am-2015-5077CCBYNCND

Burns, R.G., 1993. Rates and mechanisms of chemical weathering of ferromagnesian silicate minerals on Mars. Geochimica et Cosmochimica Acta 57, 4555–4574. doi:10.1016/0016-7037(93)90182-V

Burns, R.G., 1987. Gossans on Mars. 18th Lunar and Planetary Science Conference 713–721.
Carter, J., Poulet, F., Bibring, J.-P., Mangold, N., Murchie, S., 2013. Hydrous minerals on Mars as seen by the CRISM and OMEGA imaging spectrometers: Updated global view: HYDROUS MINERALS ON MARS: GLOBAL VIEW. Journal of Geophysical Research: Planets 118, 831–858. doi:10.1029/2012JE004145
Cavanagh, P.D., Bish, D.L., Blake, D.F., Vaniman, D.T., Morris, R.V., Ming, D.W., Rampe, E.B., Achilles, C.N., Chipera, S.J., Treiman, A.H., Downs, R.T., Morrison, S.M., Fendrich, K.V., Yen, A.S., Grotzinger, J., Crisp, J.A., Bristow, T.F., Sarrazin, P., Farmer, J.D., Des Marais, Stolper, E., Morookian, J.M., Wilson, M.A., Spanovich, N., Anderson, R., 2015. Confidence Hills Mineralogy and CheMin Results from Base of Mt. Sharp, Pahrump Hills, Gale Crater, Mars. 46th Lunar and Planetary Science Conference Abstract #2735.
Chemtob, S.M., Arvidson, R.E., FernáNdez-Remolar, D., Amils, R., 2006. Identification of Hydrated Sulfates Collected in the Northern Rio Tinto Valley by Reflectance and Raman Spectroscopy. Lunar and Planetary Science XXXVII Abstract 1941.
Clark, R.N., Roush, T.L., 1984. Reflectance spectroscopy: Quantitative analysis techniques for remote sensing applications. Journal of Geophysical Research 89, 6329. doi:10.1029/JB089iB07p06329
Dixon, E.M., Elwood Madden, A.S., Hausrath, E.M., Elwood Madden, M.E., 2015. Assessing hydrodynamic effects on jarosite dissolution rates, reaction products, and preservation on Mars: Hydrodynamics effects Mars Minerals. Journal of Geophysical Research: Planets 120, 625–642. doi:10.1002/2014JE004779
Ehlmann, B.L., Mustard, J.F., Murchie, S.L., Bibring, J.-P., Meunier, A., Fraeman, A.A., Langevin, Y., 2011. Subsurface water and clay mineral formation during the early history of Mars. Nature 479, 53–60. doi:10.1038/nature10582
Ehlmann, B.L., Mustard, J.F., Swayze, G.A., Clark, R.N., Bishop, J.L., Poulet, F., Des Marais, D.J., Roach, L.H., Milliken, R.E., Wray, J.J., Barnouin-Jha, O., Murchie, S.L., 2009. Identification of hydrated silicate minerals on Mars using MRO-CRISM: Geologic context near Nili Fossae and implications for aqueous alteration. Journal of Geophysical Research 114. doi:10.1029/2009JE003339
Elwood Madden, M.E., Bodnar, R.J., Rimstidt, J.D., 2004. Jarosite as an indicator of water-limited chemical weathering on Mars. Nature 431, 821–823. doi:10.1038/nature02971
Farrand, W.H., Glotch, T.D., Rice, J.W., Hurowitz, J.A., Swayze, G.A., 2009. Discovery of jarosite within the Mawrth Vallis region of Mars: Implications for the geologic history of the region. Icarus 204, 478–488. doi:10.1016/j.icarus.2009.07.014
Fernández-Remolar, D.C., 2003. Geological record of an acidic environment driven by iron hydrochemistry: The Tinto River system. Journal of Geophysical Research 108. doi:10.1029/2002JE001918
Fernández-Remolar, D.C., Knoll, A.H., 2008. Fossilization potential of iron-bearing minerals in acidic environments of Rio Tinto, Spain: Implications for Mars exploration. Icarus 194, 72–85. doi:10.1016/j.icarus.2007.10.009
Fernández-Remolar, D.C., Morris, R.V., Gruener, J.E., Amils, R., Knoll, A.H., 2005. The Río Tinto Basin, Spain: Mineralogy, sedimentary geobiology, and implications for interpretation of outcrop rocks at Meridiani Planum, Mars. Earth and Planetary Science Letters 240, 149–167. doi:10.1016/j.epsl.2005.09.043
Fernández-Remolar, D.C., Prieto-Ballesteros, O., Gómez-Ortíz, D., Fernández-Sampedro, M., Sarrazin, P., Gailhanou, M., Amils, R., 2011. Río Tinto sedimentary mineral assemblages: A terrestrial perspective that suggests some formation pathways of phyllosilicates on Mars. Icarus 211, 114–138. doi:10.1016/j.icarus.2010.09.008
Fialips, C.-I., Petit, S., Decarreau, A., Beaufort, D., 2000. Influence of synthesis pH on kaolinite "crystallinity" and surface properties. Clays and Clay Minerals 48, 173–184.
Gendrin, A., 2005. Sulfates in Martian Layered Terrains: The OMEGA/Mars Express View. Science 307, 1587–1591. doi:10.1126/science.1109087
Golden, D.C., Ming, D.W., Morris, R.V., Mertzman, S.A., 2005. Laboratory-simulated acid-sulfate weathering of basaltic materials: Implications for formation of sulfates at Meridiani Planum and Gusev crater, Mars. Journal of Geophysical Research 110. doi:10.1029/2005JE002451
Graff, T.G., Morris, R.V., Achilles, C.N., Agresti, A.G., Ming, D.W., Hamilton, J.C., Mertzman, S.A., Smith, J., 2012. Chemical and Mineralogical Characterization of Acid-Sulfate Alteration of

Basaltic Material on Mauna Kea Volcano, Hawaii: Jarosite and Hydrated Halloysite. Lunar and Planetary Science XLIII Abstract, 2639.

Grotzinger, J.P., Arvidson, R.E., Bell, J.F., Calvin, W., Clark, B.C., Fike, D.A., Golombek, M., Greeley, R., Haldemann, A., Herkenhoff, K.E., Jolliff, B.L., Knoll, A.H., Malin, M., McLennan, S.M., Parker, T., Soderblom, L., Sohl-Dickstein, J.N., Squyres, S.W., Tosca, N.J., Watters, W.A., 2005. Stratigraphy and sedimentology of a dry to wet eolian depositional system, Burns formation, Meridiani Planum, Mars. Earth and Planetary Science Letters 240, 11–72. doi:10.1016/j.epsl.2005.09.039

Grotzinger, J.P., Gupta, S., Malin, M.C., Rubin, D.M., Schieber, J., Siebach, K., Sumner, D.Y., Stack, K.M., Vasavada, A.R., Arvidson, R.E., Calef, F., Edgar, L., Fischer, W.F., Grant, J.A., Griffes, J., Kah, L.C., Lamb, M.P., Lewis, K.W., Mangold, N., Minitti, M.E., Palucis, M., Rice, M., Williams, R.M.E., Yingst, R.A., Blake, D., Blaney, D., Conrad, P., Crisp, J., Dietrich, W.E., Dromart, G., Edgett, K.S., Ewing, R.C., Gellert, R., Hurowitz, J.A., Kocurek, G., Mahaffy, P., McBride, M.J., McLennan, S.M., Mischna, M., Ming, D., Milliken, R., Newsom, H., Oehler, D., Parker, T.J., Vaniman, D., Wiens, R.C., Wilson, S.A., 2015. Deposition, exhumation, and paleoclimate of an ancient lake deposit, Gale crater, Mars. Science 350, aac7575–aac7575. doi:10.1126/science.aac7575

Grotzinger, J.P. et al., 2014. A Habitable Fluvio-Lacustrine Environment at Yellowknife Bay, Gale Crater, Mars. Science 343, 1242777–1242777. doi:10.1126/science.1242777

Hurowitz, J.A., Fischer, W.W., Tosca, N.J., Milliken, R.E., 2010. Origin of acidic surface waters and the evolution of atmospheric chemistry on early Mars. Nature Geoscience 3, 323–326. doi:10.1038/ngeo831

Hurowitz, J.A., Tosca, N.J., Dyar, M.D., 2009. Acid production by FeSO4{middle dot}nH2O dissolution and implications for terrestrial and martian aquatic systems. American Mineralogist 94, 409–414. doi:10.2138/am.2009.3085

Klingelhofer, G., 2004. Jarosite and Hematite at Meridiani Planum from Opportunity's Mossbauer Spectrometer. Science 306, 1740–1745. doi:10.1126/science.1104653

Langevin, Y., 2005. Sulfates in the North Polar Region of Mars Detected by OMEGA/Mars Express. Science 307, 1584–1586. doi:10.1126/science.1109091

Lichtenberg, K.A., Arvidson, R.E., Morris, R.V., Murchie, S.L., Bishop, J.L., Fernandez Remolar, D., Glotch, T.D., Noe Dobrea, E., Mustard, J.F., Andrews-Hanna, J., Roach, L.H., 2010. Stratigraphy of hydrated sulfates in the sedimentary deposits of Aram Chaos, Mars. Journal of Geophysical Research 115. doi:10.1029/2009JE003353

Madejová, J., Pentrák, M., Pálková, H., Komadel, P., 2009. Near-infrared spectroscopy: A powerful tool in studies of acid-treated clay minerals. Vibrational Spectroscopy 49, 211–218. doi:10.1016/j.vibspec.2008.08.001

Metz, J., Grotzinger, J., Okubo, C., Milliken, R., 2010. Thin-skinned deformation of sedimentary rocks in Valles Marineris, Mars. Journal of Geophysical Research 115. doi:10.1029/2010JE003593

Metz, J.M., Grotzinger, J.P., Mohrig, D., Milliken, R., Prather, B., Pirmez, C., McEwen, A.S., Weitz, C.M., 2009. Sublacustrine depositional fans in southwest Melas Chasma. Journal of Geophysical Research 114. doi:10.1029/2009JE003365

Michalski, J.R., Niles, P.B., Cuadros, J., Baldridge, A.M., 2013. Multiple working hypotheses for the formation of compositional stratigraphy on Mars: Insights from the Mawrth Vallis region. Icarus 226, 816–840. doi:10.1016/j.icarus.2013.05.024

Milliken, R.E., Swayze, G.A., Arvidson, R.E., Bishop, J.L., Clark, R.N., Ehlmann, B.L., Green, R.O., Grotzinger, J.P., Morris, R.V., Murchie, S.L., Mustard, J.F., Weitz, C., 2008. Opaline silica in young deposits on Mars. Geology 36, 847. doi:10.1130/G24967A.1

Murchie, S., Arvidson, R., Bedini, P., Beisser, K., Bibring, J.-P., Bishop, J., Boldt, J., Cavender, P., Choo, T., Clancy, R.T., Darlington, E.H., Des Marais, D., Espiritu, R., Fort, D., Green, R., Guinness, E., Hayes, J., Hash, C., Heffernan, K., Hemmler, J., Heyler, G., Humm, D., Hutcheson, J., Izenberg, N., Lee, R., Lees, J., Lohr, D., Malaret, E., Martin, T., McGovern, J.A., McGuire, P., Morris, R., Mustard, J., Pelkey, S., Rhodes, E., Robinson, M., Roush, T., Schaefer, E., Seagrave, G., Seelos, F., Silverglate, P., Slavney, S., Smith, M., Shyong, W.-J., Strohbehn, K., Taylor, H., Thompson, P., Tossman, B., Wirzburger, M., Wolff, M., 2007. Compact Reconnaissance Imaging Spectrometer for Mars (CRISM) on Mars Reconnaissance Orbiter (MRO). Journal of Geophysical Research 112. doi:10.1029/2006JE002682

Mustard, J.F., Murchie, S.L., Pelkey, S.M., Ehlmann, B.L., Milliken, R.E., Grant, J.A., Bibring, J.-P., Poulet, F., Bishop, J., Dobrea, E.N., Roach, L., Seelos, F., Arvidson, R.E., Wiseman, S., Green, R., Hash, C., Humm, D., Malaret, E., McGovern, J.A., Seelos, K., Clancy, T., Clark, R., Marais, D.D., Izenberg, N., Knudson, A., Langevin, Y., Martin, T., McGuire, P., Morris, R., Robinson, M., Roush, T., Smith, M., Swayze, G., Taylor, H., Titus, T., Wolff, M., 2008. Hydrated silicate minerals on Mars observed by the Mars Reconnaissance Orbiter CRISM instrument. Nature 454, 305–309. doi:10.1038/nature07097

Noe Dobrea, E., Michalski, J.R., Swayze, G.A., 2011. Aqueous Mineralogy and Stratigraphy at and Around the Proposed Mawrth Vallis MSL Landing Site: New Insights into the Aqueous History of the Region. The International Journal of Mars Science and Exploration 6, 32–46.

Pelkey, S.M., Mustard, J.F., Murchie, S., Clancy, R.T., Wolff, M., Smith, M., Milliken, R., Bibring, J.-P., Gendrin, A., Poulet, F., Langevin, Y., Gondet, B., 2007. CRISM multispectral summary products: Parameterizing mineral diversity on Mars from reflectance. Journal of Geophysical Research 112. doi:10.1029/2006JE002831

Poulet, F., Bibring, J.-P., Mustard, J.F., Gendrin, A., Mangold, N., Langevin, Y., Arvidson, R.E., Gondet, B., Gomez, C., Berthé, M., Bibring, J.-P., Langevin, Y., Erard, S., Forni, O., Gendrin, A., Gondet, B., Manaud, N., Poulet, F., Poulleau, G., Soufflot, A., Combes, M., Drossart, P., Encrenaz, T., Fouchet, T., Melchiorri, R., Bellucci, G., Altieri, F., Formisano, V., Fonti, S., Capaccioni, F., Cerroni, P., Coradini, A., Korablev, O., Kottsov, V., Ignatiev, N., Titov, D., Zasova, L., Mangold, N., Pinet, P., Schmitt, B., Sotin, C., Hauber, E., Hoffmann, H., Jaumann, R., Keller, U., Arvidson, R., Mustard, J., Forget, F., 2005. Phyllosilicates on Mars and implications for early martian climate. Nature 438, 623–627. doi:10.1038/nature04274

Roach, L.H., Mustard, J., Gendrin, A., Fernández-Remolar, D., Amils, R., Amaral-Zettler, L., 2006. Finding mineralogically interesting targets for exploration from spatially coarse visible and near IR spectra. Earth and Planetary Science Letters 252, 201–214. doi:10.1016/j.epsl.2006.09.044

Roach, L.H., Mustard, J.F., Swayze, G., Milliken, R.E., Bishop, J.L., Murchie, S.L., Lichtenberg, K., 2010. Hydrated mineral stratigraphy of Ius Chasma, Valles Marineris. Icarus 206, 253–268. doi:10.1016/j.icarus.2009.09.003

Sobron, P., Bishop, J.L., Blake, D.F., Chen, B., Rull, F., 2014. Natural Fe-bearing oxides and sulfates from the Rio Tinto Mars analog site: Critical assessment of VNIR reflectance spectroscopy, laser Raman spectroscopy, and XRD as mineral identification tools. American Mineralogist 99, 1199–1205. doi:10.2138/am.2014.4595

Sobron, P., Sanz, A., Acosta, T., Rull, F., 2009. A Raman spectral study of stream waters and efflorescent salts in Rio Tinto, Spain. Spectrochimica Acta Part A: Molecular and Biomolecular Spectroscopy 71, 1678–1682. doi:10.1016/j.saa.2008.06.035

Squyres, S.W., 2004. In Situ Evidence for an Ancient Aqueous Environment at Meridiani Planum, Mars. Science 306, 1709–1714. doi:10.1126/science.1104559

Sunshine, J.M., Pieters, C.M., 1993. Estimating Modal Abundances From the Spectra of Natural and Laboratory Pyroxene Mixtures Using the Modified Gaussian Model. Journal of Geophysical Research 98, 9075–9087.

Thollot, P., Mangold, N., Ansan, V., Le Mouélic, S., Milliken, R.E., Bishop, J.L., Weitz, C.M., Roach, L.H., Mustard, J.F., Murchie, S.L., 2012. Most Mars minerals in a nutshell: Various alteration phases formed in a single environment in Noctis Labyrinthus: ALTERATION PHASES IN NOCTIS LABYRINTHUS. Journal of Geophysical Research: Planets 117, n/a–n/a. doi:10.1029/2011JE004028

Tosca, N.J., 2004. Acid-sulfate weathering of synthetic Martian basalt: The acid fog model revisited. Journal of Geophysical Research 109. doi:10.1029/2003JE002218

Tosca, N.J., Knoll, A.H., McLennan, S.M., 2008a. Water Activity and the Challenge for Life on Early Mars. Science 320, 1204–1207. doi:10.1126/science.1155432

Tosca, N.J., McLennan, S.M., 2006. Chemical divides and evaporite assemblages on Mars. Earth and Planetary Science Letters 241, 21–31. doi:10.1016/j.epsl.2005.10.021

Tosca, N.J., Milliken, R.E., Michel, F.M., 2008b. Smectite Formation on Early Mars: Experimental Constraints. Martian Phyllosilicates: Recorders of Aqueous Processes Abstract, 7030.

Vaniman, D.T. et al., 2014. Mineralogy of a Mudstone at Yellowknife Bay, Gale Crater, Mars. Science 343, 1243480–1243480. doi:10.1126/science.1243480

Wang, A., Korotev, R.L., Jolliff, B.L., Haskin, L.A., Crumpler, L., Farrand, W.H., Herkenhoff, K.E., de Souza, P., Kusack, A.G., Hurowitz, J.A., Tosca, N.J., 2006. Evidence of phyllosilicates in Wooly Patch, an altered rock encountered at West Spur, Columbia Hills, by the Spirit rover in Gusev crater, Mars. Journal of Geophysical Research 111. doi:10.1029/2005JE002516

Weitz, C.M., Bishop, J.L., Thollot, P., Mangold, N., Roach, L.H., 2011. Diverse mineralogies in two troughs of Noctis Labyrinthus, Mars. Geology 39, 899–902. doi:10.1130/G32045.1

Weitz, C.M., Noe Dobrea, E., Wray, J.J., 2014. Mixtures of clays and sulfates within deposits in western Melas Chasma, Mars. Icarus. doi:10.1016/j.icarus.2014.04.009

Figures

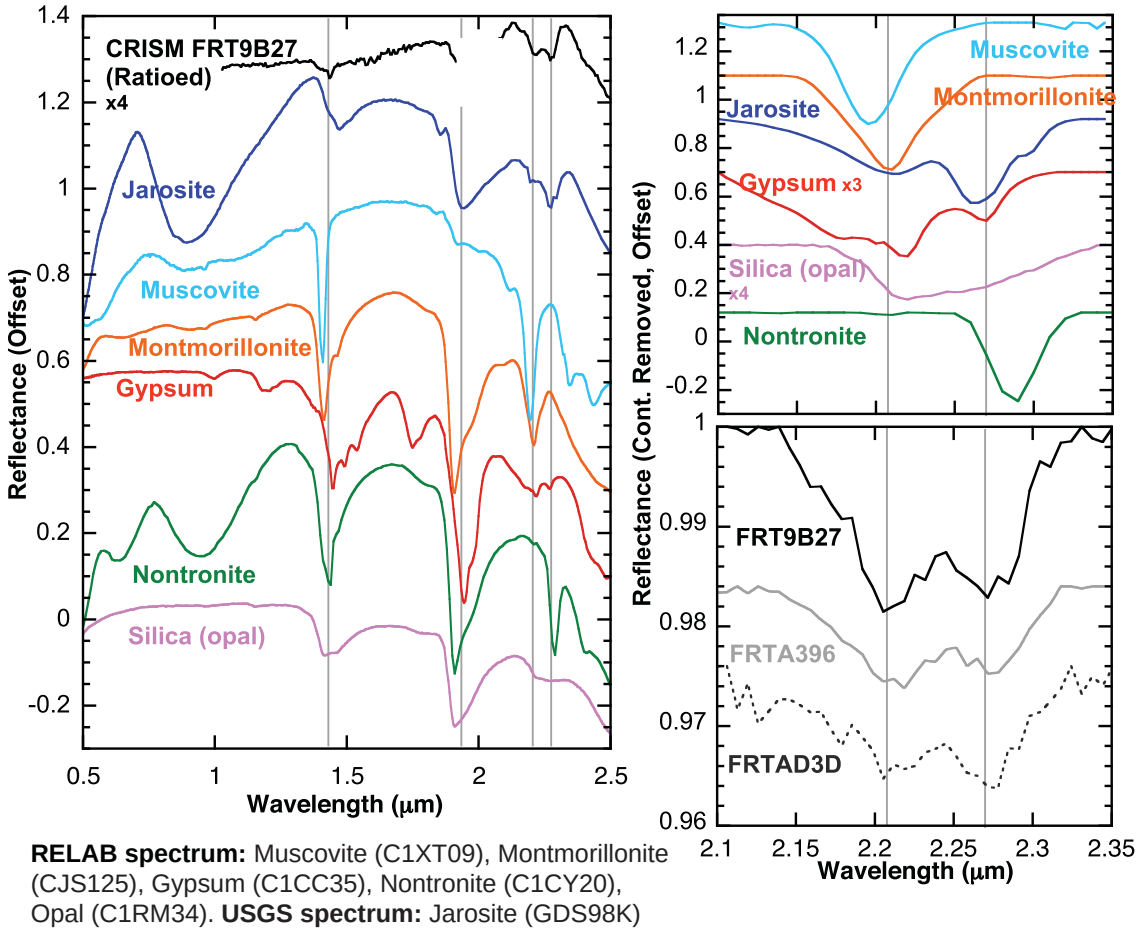

RELAB spectrum: Muscovite (C1XT09), Montmorillonite (CJS125), Gypsum (C1CC35), Nontronite (C1CY20), Opal (C1RM34). **USGS spectrum:** Jarosite (GDS98K)

Figure 1: Reflectance spectra of minerals with absorptions between 2.2 and 2.3 μm (source: RELAB database) are compared to CRISM spectra showing the 'doublet' absorption. Continuum-removed spectra from 2.1 to 2.35 μm (right) are shown to highlight absorption features in the wavelength region where the doublet occurs. None of the pure mineral spectra have absorption positions and depths that are a direct match to the doublet absorptions, thus a mineral mixture is implied.

Sample ID	Location	Terrace	Spectral Doublet	Reitveld Refinement
RT1	Berrocal	Modern		
RT2	Berrocal	Modern		
RT3	Berrocal	Modern		
RT4 (mud, loose)	Berrocal	Modern		
RT5	Anabel's Garden, Upper Road	N/A		
RT6	Anabel's Garden, Upper Road	N/A		
RT7	Anabel's Garden, Upper Road	N/A		Yes
RT8	Anabel's Garden, Upper Road	N/A		
RT9	Anabel's Garden, Upper Road	N/A	Yes	Yes
RT10	Anabel's Garden, Upper Road	N/A	Yes	Yes
RT11	Anabel's Garden, Upper Road	N/A	Yes	Yes
RT12	Barranco de los Locos	Lower Terrace	Yes	Yes
RT13	Barranco de los Locos	Lower Terrace		
RT14	Barranco de los Locos	Lower Terrace		
RT15	Barranco de los Locos	Lower Terrace	Yes	Yes
RT16	Anabel's Garden, Stream 1	Modern	Yes	Yes
RT17 (precipitate)	Anabel's Garden, Stream 2	Modern		
RT18 (precipitate)	Anabel's Garden, Stream 2	Modern		
RT19	Anabel's Garden, Stream 2	Modern	Yes	Yes
RT20 (precipitate)	Anabel's Garden, Stream 2	Modern		
RT21	Anabel's Garden, Stream 2	Modern		
RT22	Anabel's Garden, Stream 2	Modern		
RT23	Anabel's Garden, Stream 2	Modern		Yes
RT24	Source Spring	Modern		
RT25	Source Spring	Modern		
RT26	Source Spring	Modern	Yes	Yes
RT27 (precipitate)	Source Spring	Modern		
RT28	Alta de la Mesa	Upper Terrace		
RT29	Alta de la Mesa	Upper Terrace		
RT30	Alta de la Mesa	Upper Terrace		Yes
RT31	Alta de la Mesa	Upper Terrace		
RT32	Gossan outcrop	N/A		
RT33	Gossan outcrop	N/A		
RT34	Gossan outcrop	N/A		

Table 1: A full list of samples collected at the modern streambed, lower and upper terraces at Rio Tinto. All samples are rocks unless otherwise noted. Each sample is measured with the ASD, FTIR, and XRD in the laboratory. Samples with a spectral doublet and those that have been analyzed with a Rietveld refinement are noted.

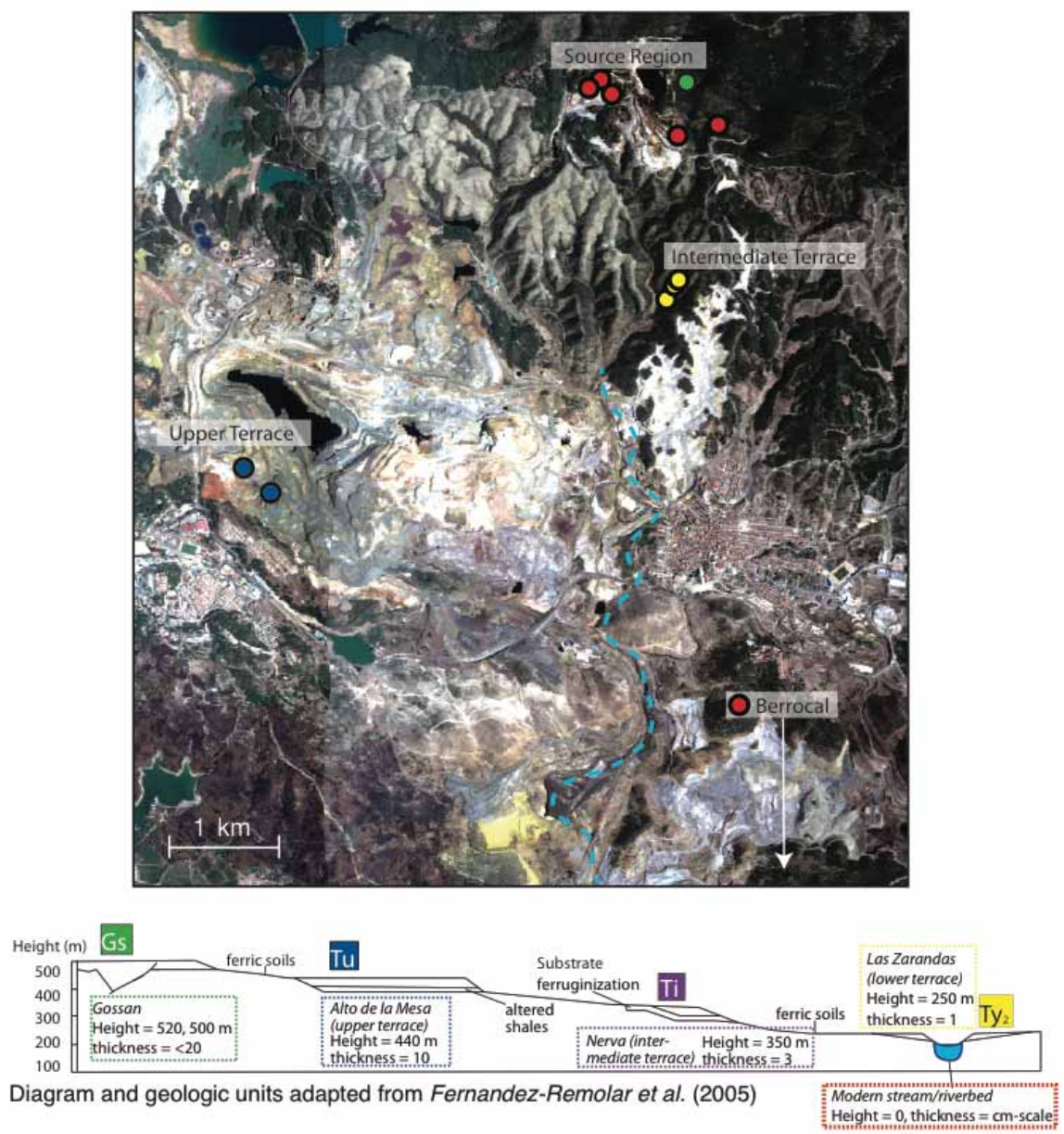

Figure 2: Terraces of the Rio Tinto in the schematic diagram from Fernandez-Remolar et al. (2005) are matched with locations in the HyMap aerial hyperspectral image of the region that were sampled in this study.

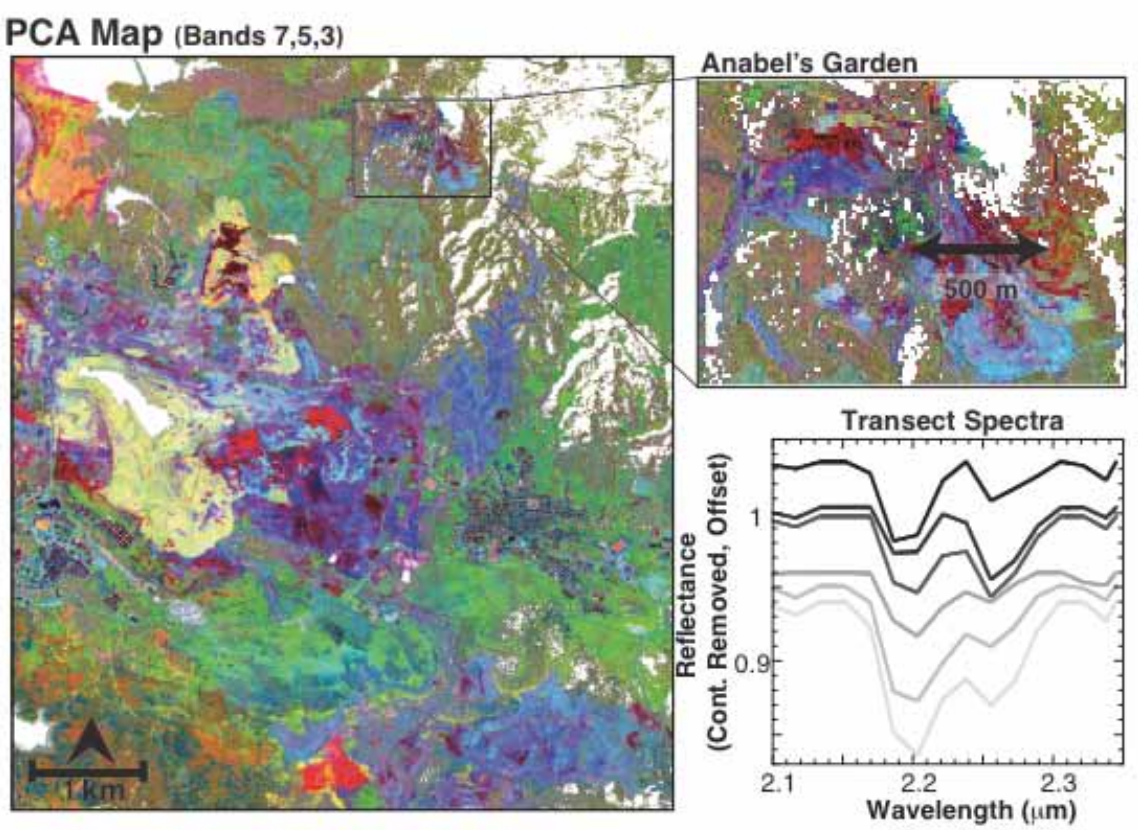

Figure 3: A principal components analysis has been carried out on the same HyMap image as seen in Figure 2, and like colors in the image correspond to regions of spectral similarity (R = PCA band 7, G = band 3, B = band 5). The spectral doublet is associated with units that appear in a dark red color in this false-color image, which is particularly evident at Anabel's Garden (inset) where a number of the doublet-bearing samples were collected. Variation in the spectral doublet from 2.2 – 2.3 μm is highlighted with spectra collected from a 500 m HyMap transect (black arrow).

Sample			Rietveld Results				XRD Peak Areas	
Sample	Location	Doublet?	Jarosite (wt%)	Muscovite (wt%)	Illite (wt%)	R_{wp}	Peak area: Musc/Ill	Peak area: Jarosite
RT9	AG Mining Terrace	Yes	3	16	14	5.61	1717.8	639
RT10	AG Mining Terrace	Yes	7	46	0	5.01	2438.3	673.4
RT11	AG Mining Terrace	Yes	4	24	0	5.52	1239.4	573.1
RT12	Barranco de los Locos	Yes	11	13	0	1.12	2115.3	1956.1
RT15	Barranco de los Locos	Yes	37	12	0	1.21	2089.9	2050.9
RT16	Anabel's Garden (Stream)	Yes	3	5	0	10.08	555.4	353.4
RT19	Anabel's Garden (stream)	Yes	3	0	19	3.16	536.3	464.9
RT26	Source Spring	Yes	8	50	0	2.52	4655.9	2959.1
RT30	Alta de la Mesa	No	0	0	0	3.67	0	0
RT23	Anabel's Garden (Stream)	No	32	0	0	1.66	0	1003.8
RT7	Anabel's Garden	No	0	0	4	1.03	432.1	0

Table 2: Sample IDs and origin of samples that were analyzed using XRD and reflectance spectroscopy. The jarosite and Al-clay (muscovite/illite) content of each sample was estimated using Rietveld refinement on the XRD patterns.

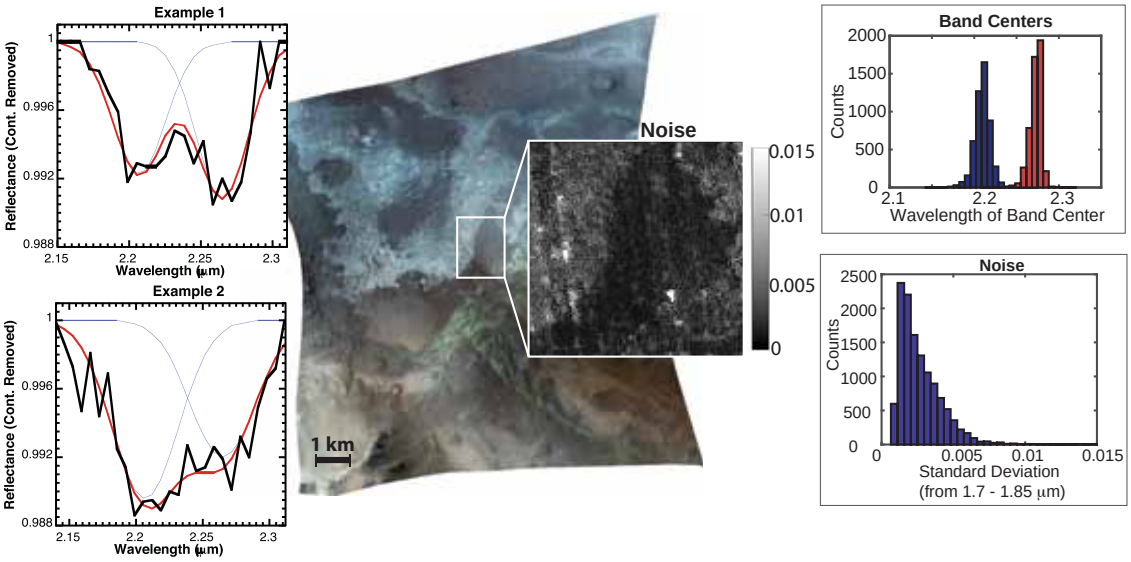

Figure 4: Two Gaussian fit examples are shown for FRT00009B27 from Ius Chasma, Mars. Due to noise in the spectrum, the Gaussian mean may be a better representative of band depth minimum than the true reflectance value. Noise and spectral smile are further analyzed for a central subset of the image. Noise is calculated as the standard deviation of a flat, absorption free portion of the spectrum from 1.7 – 1.85 μm. An image and histogram of this standard deviation show that noise is typically < 0.005 in reflectance. Band center histograms are also shown for the central image subset, and the reduced spread in band centers compared to the full image suggests spectral smile plays a role in the band center position.

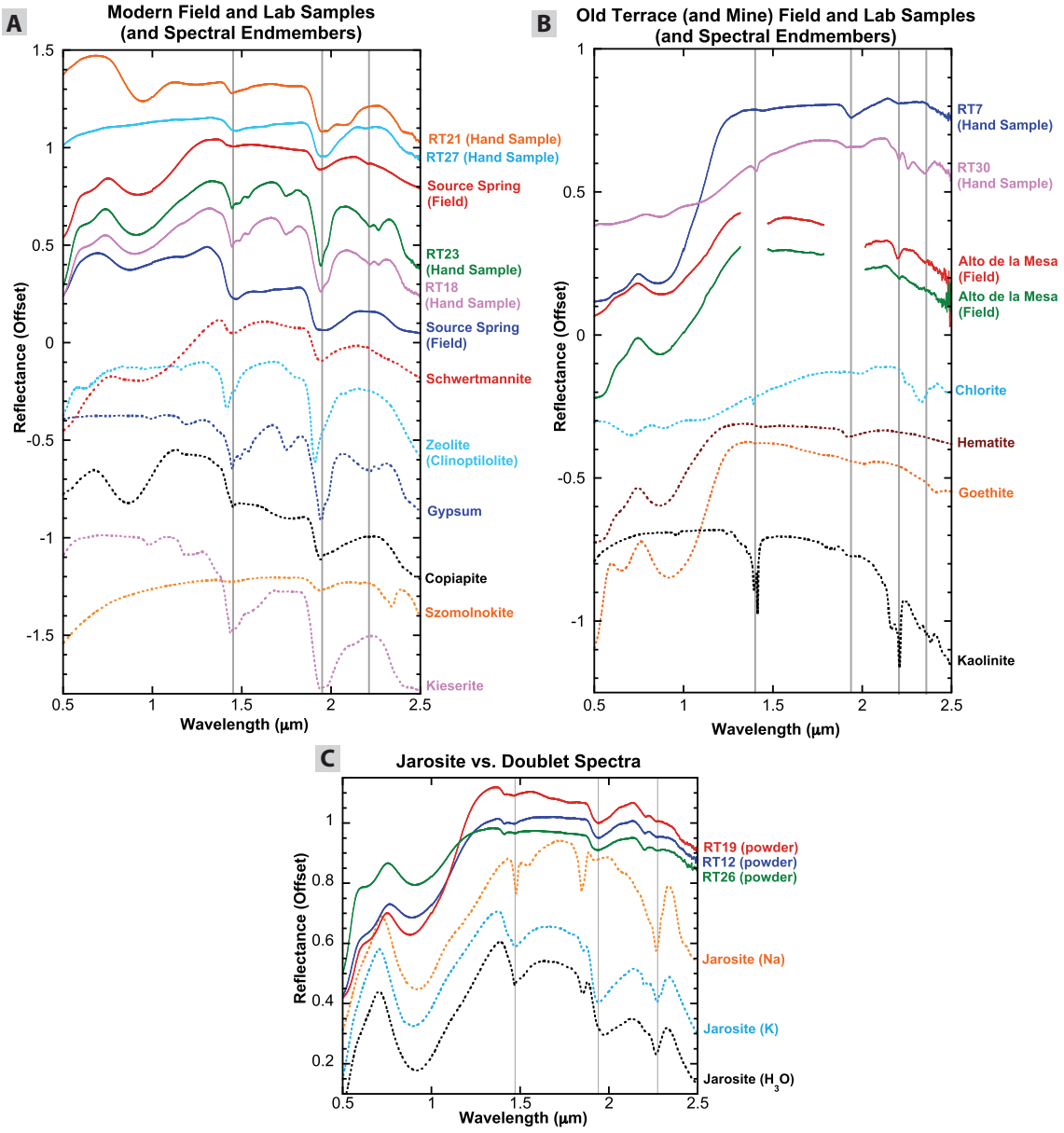

Figure 5: Example spectra from the field and laboratory for the A) modernly precipitating streambed at Rio Tinto (source region, which includes Source Spring, Richi Spring, and Anabel's Garden) and B) the ~2myr old terrace at Alto de la Mesa. These spectra show the transition from very hydrated, sulfate minerals to ferric oxides through time (with some clays possibly associated with mining activity). All of the mineralogies identified in hand samples are also found in the field spectra, but only a limited number of each is shown for the sake of clarity. In C), absorptions in powdered samples that show a doublet are specifically compared to jarosite spectral endmembers. Again, a very similar doublet signature is seen in both field and hand samples, but is not shown for clarity. Endmember mineral spectra from RELAB and USGS are shown for reference (RELAB: RM-JFM-036, RM-JFM-035, CC-JFM-013A, JB-JLB-752, JB-JLB-753, JB-JLB-757, JB-CMP-047, JB-CMP-054, CC-JFM-

017-B, JB-JLB_256, CC-JFM-035, CL-TXH-014, JB-CMP-25-B; USGS: BZ93-1, GDS2 Zeolite W1R1Bb)

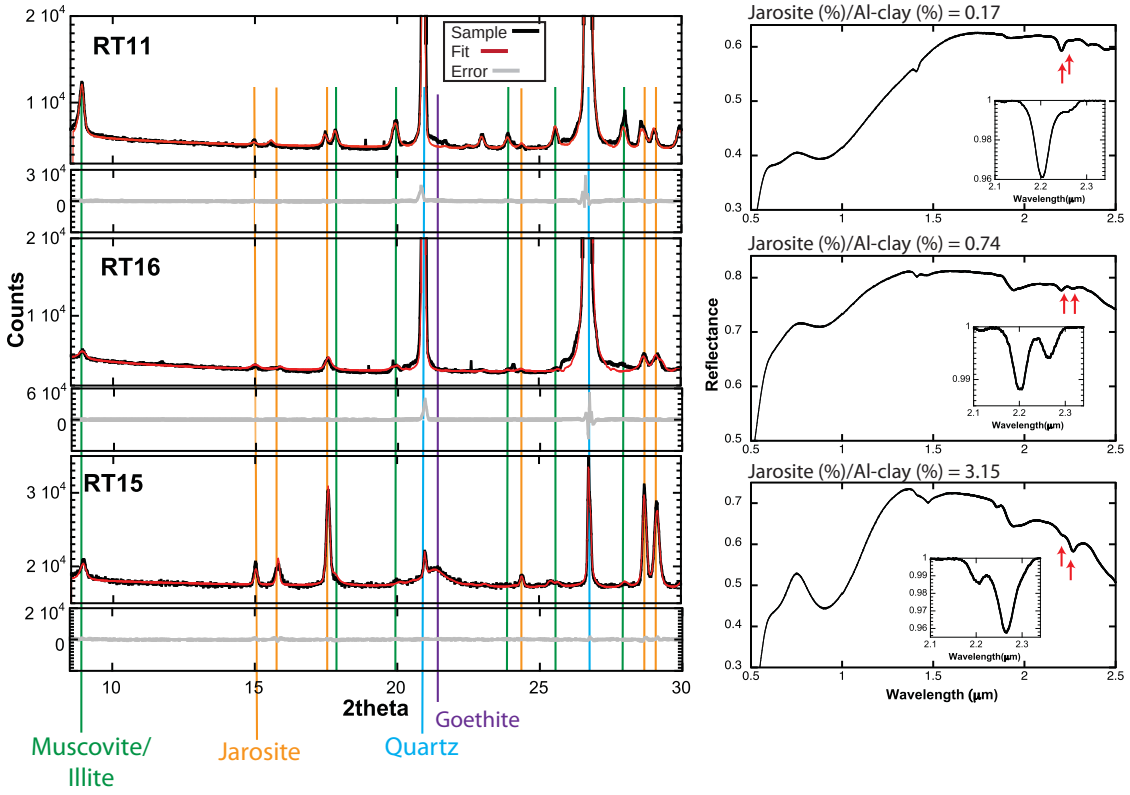

Figure 6: XRD patterns with corresponding reflectance spectra from three powdered samples with different proportions of jarosite and Al-clay (RT 11, RT15, RT16). Major phases are labeled for the XRD patterns and absorptions corresponding to the doublet feature are marked by red arrows in the reflectance spectra plots.

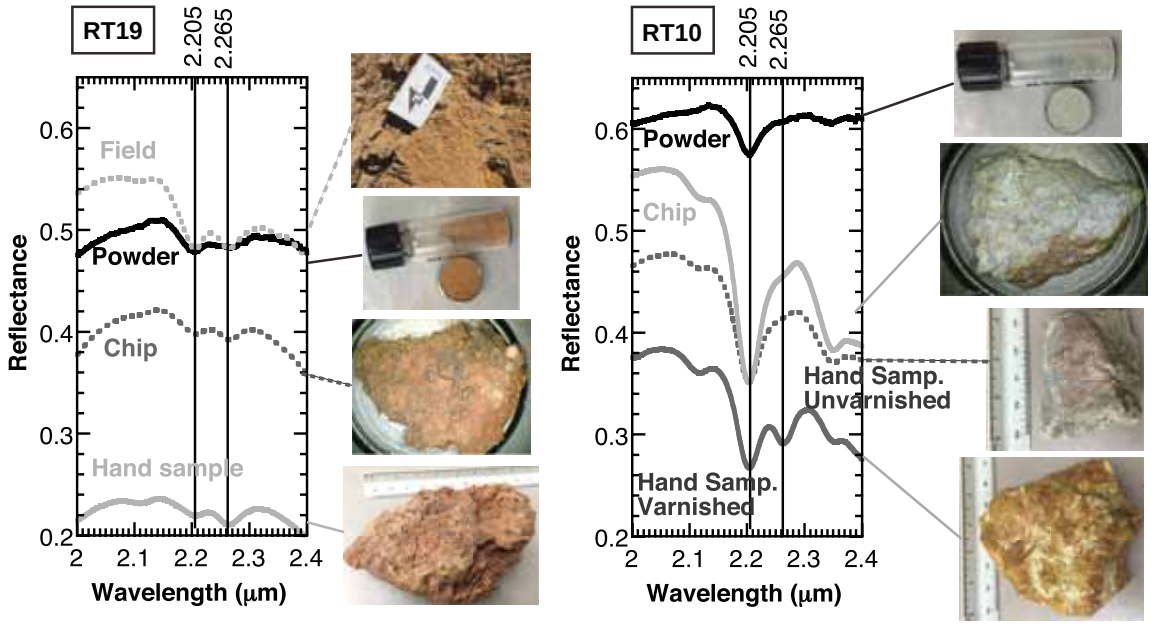

Figure 7: Example reflectance spectra acquired in the field and for hand sample, chip, and powder versions of two samples from different locations within the study region. Chips are <9 mm in diameter and powders were sieved to <45 μm. Spectra of these samples highlight the variation in absolute reflectance and band depth of the two absorptions in the doublet feature when measured at different spatial scales. Hand sample RT10 has a varnished surface for which the reflectance spectra exhibit a clear doublet feature, whereas spectra from the interior portions exhibit a much weaker long-wavelength (jarosite) absorption.

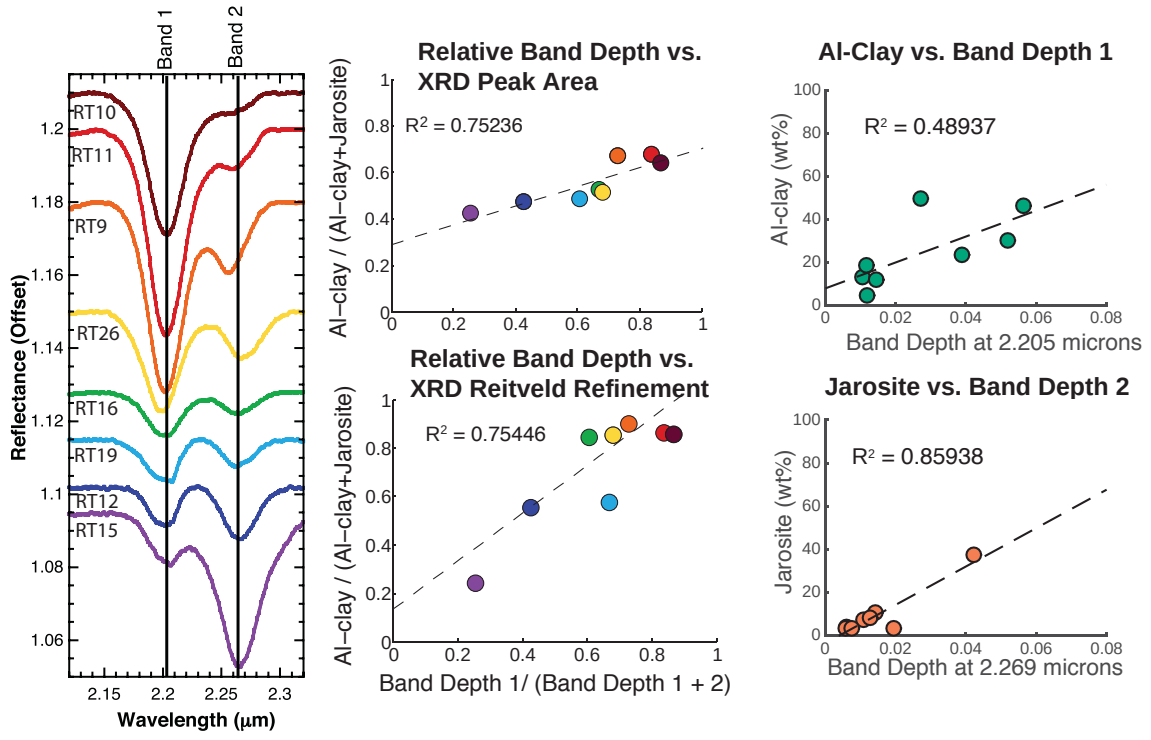

Figure 8: Comparison of XRD results with reflectance spectra (band depths) to show relationship between mineral abundances and the absorption feature strength. A direct relationship between relative amounts of jarosite and Al-clay and the strengths of the absorption features indicates the shorter wavelength absorption (band 1; ~2.21 μm) arises from Al-clay and the longer wavelength absorption (band 2; ~2.265) arises from the presence of jarosite. This suggests that relative band strengths are directly related to the relative proportions of the phyllosilicate and sulfate components.

Image	Band 1 (μm)	2σ (μm)	Band 2 (μm)	2σ (μm)
Mars				
FRT00009B27 full image	2.2109	0.0264	2.2709	0.019
FRT00009B27 center	2.2006	0.0134	2.265	0.0112
FRT0000A396 full image	2.2048	0.0154	2.2696	0.0132
FRT0000A396 center	2.2055	0.0134	2.2705	0.0136
FRT0000AD3D full image	2.2055	0.0188	2.2662	0.0156
FRT0000AD3D center	2.2085	0.0142	2.2671	0.0108
Rio Tinto				
HyMap	2.2025	0.013	2.2602	0.011

Table 3: The results of Gaussian fits for every pixel in three CRISM images (Mars) and the HyMap image (Rio Tinto) that includes the mean band centers and the 2σ deviations on these band centers. A central subset of the CRISM images is also analyzed and reported results show a shift in band centers and a decrease in standard deviation.

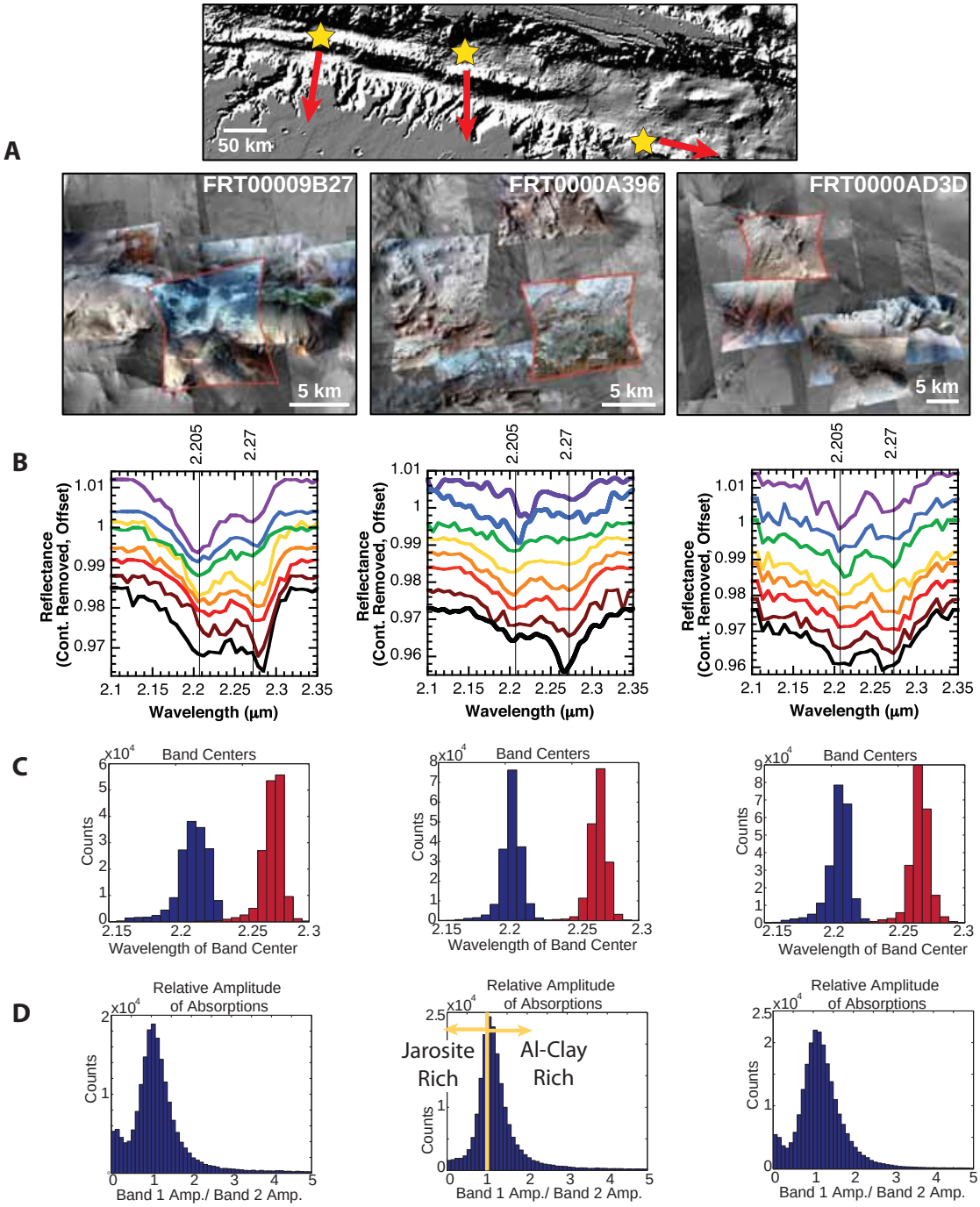

Figure 9: Examples of doublet-bearing materials on Mars as observed in MRO CRISM images. (A) MOLA hillshade image showing the location of three study regions in Ius and Melas Chasma within the Valles Marineris. Zoom-in regions below show locations of CRISM images FRT00009B27, FRT0000A396, and FRT0000AD3D in context with nearby CRISM images (overlain on HiRISE and CTX images). Doublet-bearing units in CRISM images 9B27 and AD3D are light toned and tend to drape pre-existing topography; CRISM image A396 shows that the doublet-bearing

material corresponds to a blocky, brecciated unit. (B) Examples of spectral variation within the doublet-bearing units, ranging from a stronger 2.205 μm absorption to a stronger 2.269 μm absorption. (C) Histograms showing positions of the 2.205 μm (blue) and 2.269 μm (red) band positions for every doublet-bearing pixel in each of the three images and (D) histograms showing the relative strength of the two absorption features (Band 1 = ~2.205 μm; Band 2 = ~2.269 μm). Values in (C) and (D) are based on Gaussian fits as described in the text. Data for each column in (B), (C), and (D) correspond to the CRISM FRT images labeled and highlighted in red in (A).

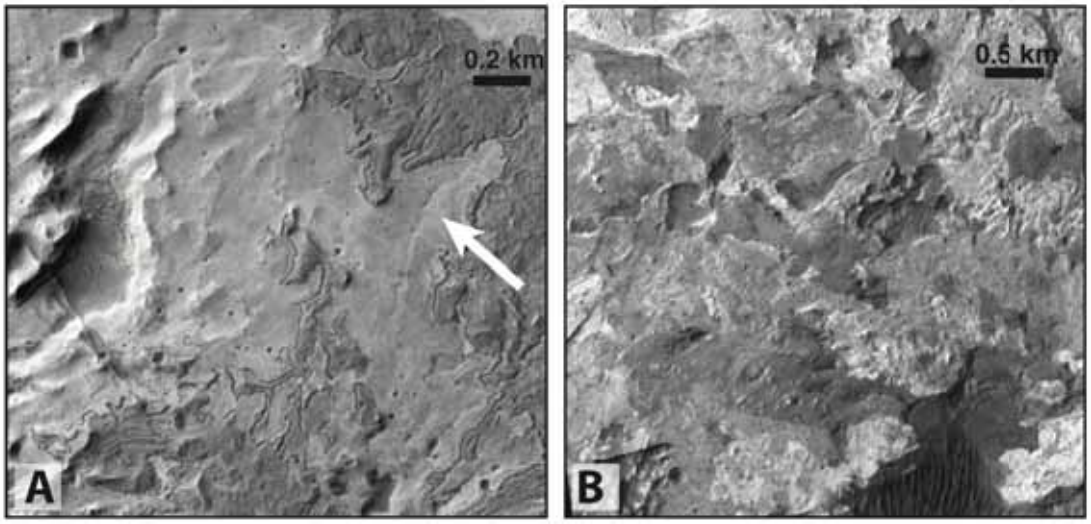

Figure 10: Examples of doublet-bearing units as observed in MRO HiRISE images. These units are typically light-toned, contorted and/or blocky in nature. (A) Example of a doublet-bearing unit in Melas Chasma that drapes pre-existing topography and spans a wide range in elevation. (B) An example of doublet-bearing, light-toned units that may have slumped off the canyon walls and are now part of a brecciated unit on the floor. The morphology and spectral characteristics of these and similar deposits are described in detail in Roach et al. (2010), Metz et al. (2010), and Weitz et al. (2014). (HiRISE images: (A) PSP_007074_1725, (B) PSP_007509_1720).

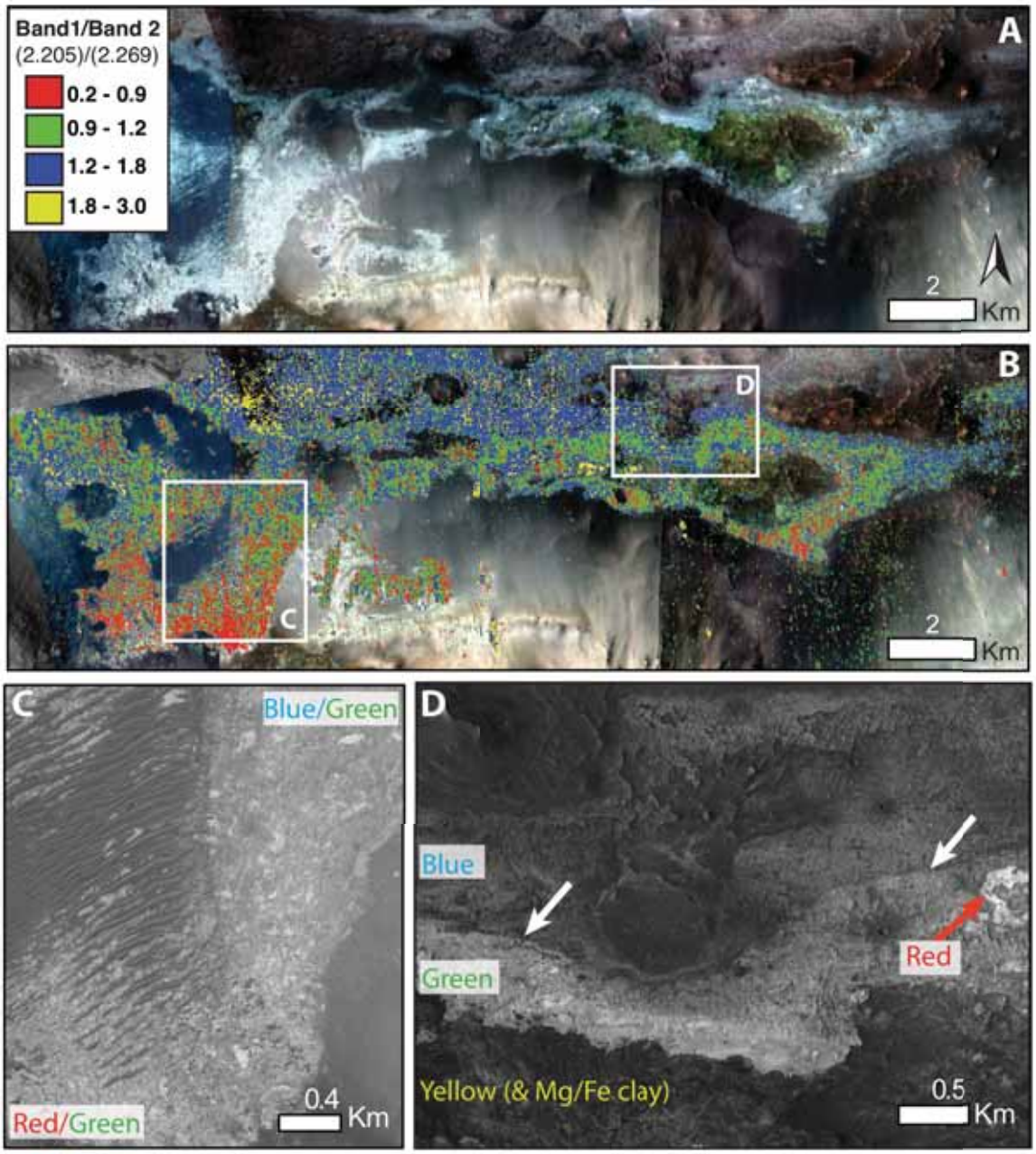

Figure 11: Relative amplitude of absorptions (band depth at 2.207/ band depth at 2.269) in Ius Chasma and associated morphology. (A) False-color CRISM images (R – band 253, B – band 53, G = band 17, top) overlain on a CTX mosaic. Fe/Mg-clay bearing regions appear greenish in color and the doublet-bearing regions appear light-toned or white. (B) CRISM pixels with the doublet feature are highlighted by different colors that map the relative band strength of the two absorptions, with a gradient from more jarosite rich (red), to roughly equal jarosite/Al-phyllosilicate strength, to slightly more Al-phyllosilicate rich (blue), to very Al-phyllosilicate rich (yellow). (C) Close-up view of HiRISE image ESP_041121_1725 showing that there is no clear stratigraphic boundary associated with the transition from a more jarosite-

rich “red” region to a more Al-phyllosilicate rich “blue” area in this location. (D) Close-up of HiRISE image PSP_007074_1725 showing an example where morphologically and stratigraphically distinct units correspond to the different relative band strengths. Here, white arrows indicate a clear stratigraphic boundary that also corresponds to a clear boundary between green and blue pixels seen in (B) (HiRISE images: ESP_041121_1725, PSP_007074_1725, CRISM images listed above).

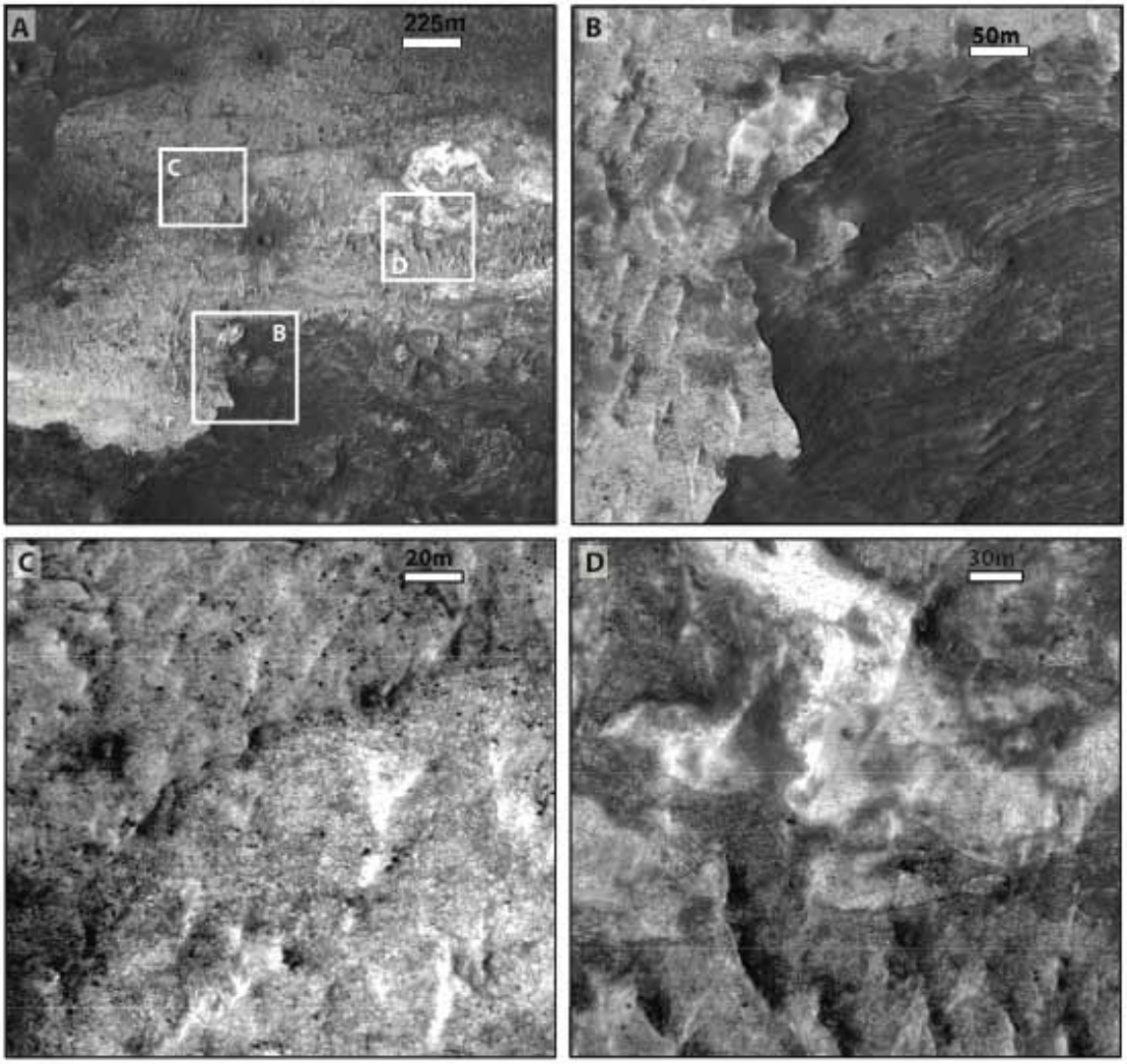

Figure 12: Evidence of the stratigraphic contacts between different doublet-bearing units that are identified as more jarosite- or Al-phyllosilicate-rich in the color map in Figure 11. (A) Context map from HiRISE image ESP_041121_1725 showing locations where three contacts are visible. (B) Shows the clay bearing unit (dark-toned, stratified with tilted bedding) unconformably overlain by the light-toned doublet unit, which has relative band strengths between 0.9 and 1.2 (i.e. the strength of the two absorptions in the doublet are similar). Next, in (C) there is a contact between this same light-toned unit and a slightly darker, more Al-phyllosilicate-rich unit, which appears to lie stratigraphically above it. Finally, (D) shows the contact between the brightest unit, which outcrops in smaller areas throughout Ius, and the

light-toned doublet-bearing unit shown in (B) and (C). This bright unit is mapped as being more jarosite rich in Figure 8 and appears to be stratigraphically lower than the light-toned unit. It is not possible to determine the exact relationship between this bright material and the dark, stratified clay deposit in this location, but in other regions it appears as if the brightest (jarosite-rich) material is stratigraphically above the clay-bearing strata. Therefore, the increasing stratigraphic order appears to be: dark (clay-bearing) strata > brightest unit > light-toned unit > moderate-toned unit. The corresponding mineralogy is consistent with: clay-rich > more jarosite-rich > equal Al-phyllosilicate and jarosite > more Al-phyllosilicate rich (that is, within the doublet-bearing units the proportion of jarosite *decreases* upsection).

Supplementary Material

1. Methods

Additional information from the methods section can be found here.

1.1. CRISM image processing and Gaussian fitting

CRISM image cubes were corrected for atmospheric gases using the 'volcano scan' method described by Langevin et al. [2005] and Mustard et al. [2008]. All CRISM processing steps, including map-projection, were carried out with the freely available IDL CRISM Analysis Tools (CAT) [Pelkey et al., 2007] and the commercially available ENVI software package.

CRISM spectra in regions of interest (ROIs) spanning ~100 to 1000 pixels were averaged to understand large-scale regional mineral assemblages. A spectrally

bland or neutral ROI was chosen to represent background martian surface reflectance properties (e.g. martian dust), and every pixel within an image was divided by the spectrum corresponding to the neutral ROI within that same image. This method produces spectral ratios that highlight and accentuate reflectance properties of ROIs relative to those associated with typical martian dust and/or soil.

Starting with the continuum-removed CRISM images, pixels whose spectra exceeded a user-defined (and image-dependent) band depth threshold at ~2.205 μm were selected for Gaussian fitting. The threshold used here is band depth ≥0.005. Though it is not suggested that the same value can be used for every CRISM image due to differences in noise, for the images used in this study this value is larger than the background 'noise' in the ratio spectra. This was determined by calculating the mean and standard deviation over the 1.70-1.85 μm wavelength range (24 channels) for each ratio spectrum (pixel) in each CRISM image. This wavelength range was chosen because it corresponds to a 'flat' portion of the spectrum for materials in these CRISM images (i.e., there are no strong absorption features within this range).

Gaussian mean (band center), standard deviation (band width), and amplitude (band strength) are allowed to vary within user-defined ranges. The Gaussian fits for at least 10 individual pixels are inspected for each image to ensure that the model fits are appropriate and residuals values for the spectral fits are reported for every pixel.

1.2 Field Observations

The ASD FieldSpec 3 collects reflected radiation through a fiber optic cable that is connected to three detectors within the spectrometer housing. The bare fiber optic cable has a field of view (FOV) of ~25° but can be equipped with different foreoptics to reduce the FOV to as small as 1°. Field spectra measured at Rio Tinto using solar radiation were acquired using a 5° FOV foreoptic with a typical standoff distance of ~1 m from the target of interest. The contact probe uses an internal quartz-tungsten-halogen (QTH) bulb for illumination and measures a spot size of ~10 mm. The contact probe has the advantage that viewing/illumination geometry is fixed and thus identical for all measurements.

1.3 Laboratory Reflectance Measurements

The light source for the laboratory reflectance measurements with the ASD FieldSpec consisted of an enclosed QTH bulb in combination with a fiber optic cable that has a 25° FOV. The source fiber was positioned to have a central incidence angle of 30° (from normal) and the receiving fiber (attached to the spectrometer) was positioned to have a central emergence angle of 0°. The heights of the fibers were adjusted as needed in order to fully illuminate and capture the entire sample in the field of view.

1.4 XRD Measurements and Rietveld Modeling

The D2 Phaser is equipped with a low voltage Cu source and a Lynxeye 1-D detector. Measurements were made using a 0.6mm divergence slit, 3 mm antiscatter shield, 2.5˚soller slit and Ni filter and rotating stage (15 rpm).

The Rietveld modeling incorporated instrumental parameters included the Cukα5_Berger emission profile, a 3rd order Chebyshev polynomial (background modeling), and specimen displacement correction. Strain and crystallite size broadening were varied to help fit the peak breadths while unit cell parameters and cation occupancies within each crystal structure were refined to model the appropriate peak position. A spherical harmonics correction was also applied to correct for any intensity variations due to preferred orientation during sample mounting.

Mineral	Source
Chlorite	Zanazzi et al. (2007)
Goethite	Yang et al. (2006)
Gypsum	Boeyens and Ichharam (2002)
Illite	Gaultieri (2000)
Jarosite	Basciano and Peterson (2007, 2008); Scarlett et al. (2010)
Muscovite	Birgatti et al. (1998); Birle and Tettenhorst (1968)
Pyrite	Bayliss (1977)
Quartz	Levien et al. (1980)

S Table 1: Structure file references for the Rietveld refinement.

References:

Basciano, L.C., Peterson, R.C., 2008. Crystal chemistry of the natrojarosite-jarosite and natrojarosite-hydronium jarosite solid-solution series: A synthetic study with full Fe site occupancy. American Mineralogist 93, 853–862. doi:10.2138/am.2008.2731

Basciano, L.C., Peterson, R.C., 2007. Jarosite hydronium jarosite solid-solution series with full iron site occupancy: Mineralogy and crystal chemistry. American Mineralogist 92, 1464–1473. doi:10.2138/am.2007.2432

Bayliss, P., 1977. Crystal structure refinement of a weakly anisotropic pyrite. American Mineralogist 62, 1168–1172.

Birle, J.D., 1968. Refined Muscovite Structure. Mineralogical Magazine 36, 883–886. doi:10.1180/minmag.1968.036.282.24

Boeyens, J.C.A., Ichharam, V.V.H., 2002. Redetermination of the crystal structure of calcium sulphate dihydrate, CaSO4 · 2H2O. Zeitschrift für Kristallographie - New Crystal Structures 217. doi:10.1524/ncrs.2002.217.jg.9

Brigatti, M.F., Frigieri, P., Luciano, P., 1998. Crystal chemistry of Mg-, Fe-bearing muscovites 2M1. American Mineralogist 83, 775–785.

Gualtieri, A.F., 2000. Accuracy of XRPD QPA using the combined Rietveld–RIR method. Journal of Applied Crystallography 33, 267–278. doi:10.1107/S002188989901643X

Levien, L., Prewitt, C.T., Weidner, D.J., 1980. Structure and elastic properties of quartz at pressure. American Mineralogist 65, 920–930.

Ransom, B., Bennett, R.H., Baerwald, R., Shea, K., 1997. TEM study of in situ organic matter on continental margins: occurrence and the “monolayer” hypothesis. Marine Geology 138, 1–9. doi:10.1016/S0025-3227(97)00012-1

Scarlett, N.V.Y., Grey, I.E., Brand, H.E.A., 2010. Ordering of iron vacancies in monoclinic jarosites. American Mineralogist 95, 1590–1593. doi:10.2138/am.2010.3591

Yang, H., Lu, R., Downs, R.T., Costin, G., 2006. Goethite, α-FeO(OH), from single-crystal data. Acta Crystallographica Section E Structure Reports Online 62, i250–i252. doi:10.1107/S1600536806047258

Zanazzi, P.F., Montagnoli, M., Nazzareni, S., Comodi, P., 2007. Structural effects of pressure on monoclinic chlorite: A single-crystal study. American Mineralogist 92, 655–661. doi:10.2138/am.2007.2341